Added resistance and seakeeping performance of trimarans in oblique waves

Jiaye Gong[a], Shiqiang Yan[b], Qingwei Ma*[b], Yunbo Li[a],

[a] College of Ocean Science and Engineering, Shanghai Maritime University, China
[b] School of Mathematics, Computer Science and Engineering, City, University of London
*Corresponding Author: q.ma@city.ac.uk

Abstract: Trimaran added resistance and seakeeping performance in oblique waves with strong nonlinearity are rarely investigated. This paper presents the numerical investigations on them by applying a hybrid method, called the QaleFOAM. This method can simulate a trimaran moving in a large wave field, considering viscous effects and dealing with violent wave-structure interaction (WSI). The numerical method is validated by experimental data for a trimaran moving in waves. Various cases are investigated with different wave steepness, different wavelengths, different forward speeds and different incident wave angles to study the properties and characteristics of the added resistance and seakeeping performance of a trimaran. The results demonstrate that the variational trend of the added resistance and motion amplitudes of the trimaran in waves is significantly affected by the wave steepness and wave incident angles and different from those of traditional mono-hull ships.

Key Words: trimaran; added resistance; seakeeping performance; oblique waves; CFD; QALE-FEM; QaleFOAM; breaking waves.

1 Introduction

Trimaran is one of the good-performance ships. It is composed of one center (main) hull and two side hulls (Pattison *et al*., 1994, Zhang 1997). The displacement of the side hulls is relatively small, e.g., about 10% of the center hull displacement (Brizzolara *et al*. 2003). Such layout has been proven to improve the lateral stability and energy efficiency of the trimaran. Various trimarans, such as RV Triton and Benchijigua Express, have been built worldwide for different purposes. As for all other ships, the added resistance due to waves and the wave-induced motions are key factors to be concerned in the design and operation of the trimaran.

Seakeeping performances of trimarans with different layouts of side hulls have been investigated. Considerable effort has been devoted to investigate the effects of the hull geometry/layout on the seakeeping performance of trimarans. Kurultay (2003) applied the potential theory and the Rankine

source method to analyze the motion responses of a trimaran with different forward speeds and different layouts of the hulls. They found that the layout with the fore and aft placement of side hulls and a lower side-to-main hull separation could improve the seakeeping performance, and the motion response of the trimaran could become more complex as Froude number (Fr) increases. Bulian *et al.* (2008) employed the potential theory to investigate the roll motion of a trimaran and concluded that the use of slim hulls can reduce the resistance but result in negative effects on the seakeeping performance. By testing three trimaran models, Hebblewhite *et al*. (2007) concluded that the longitudinal position of the side hulls plays a critical role on the seakeeping performance of the trimaran in head waves. Ma *et al.* (2012) applied a 2.5D potential method to predict the motion responses of the trimaran in oblique regular waves. Khoob *et al.* (2017), also using a potential method, investigated the effect of the long-term extreme wave loads on the lateral structure of a trimaran and observed that the asymmetric side hull can improve the seakeeping performance in head seas, whereas the symmetric side hull might perform better in oblique waves. Compared with the mono-hull ships, the behaviors of a trimaran are more likely affected, in particular in oblique waves, by nonlinear phenomena, such as significant variation of wetted area, intermittent emergence of side hulls, water spray and green water, as confirmed by experimental studies (Pastoor *et al.*, 2004; Onas *et al.*, 2011). The nonlinear phenomenon cannot be fully dealt with by potential methods. Some researchers have made efforts in studying the seakeeping performance of trimarans by Computational Fluid Dynamics (CFD) simulations. Sato *et al.* (2006) presented their CFD simulating results of heave, pitch and roll for a trimaran in oblique waves with small steepness, and demonstrated seakeeping performance of their trimaran was better than the mono hull. Ghadimi *et al* (2019) studied the effects of side hulls arrangement on the heave, roll and pitch motions of a trimaran, also subjected to linear oblique waves, by carrying out CFD simulations. Very recently, Nowruzi et al (2020a and 2020b) investigated responses of a trimaran in head waves numerically and experimentally.

In the aspect of the added resistance, related studies for trimarans in oblique waves are rarely seen in literatures. Nevertheless, the published work on the characteristics of the added resistance on other types of ships, e.g. the traditional mono-hull ships, built a good basis for the studies on the trimaran. For this purpose, some literatures on mono-hull ships are also discussed here for completeness. Afshar *et al.* (2017) applied the Neumann-Kelvin linearization to calculate the added resistance of two ship models by using a far-field method and compared their result with WAMIT results. Riesner *et al.* (2018) investigated the nonlinear effects on the added resistance by the

boundary element method (BEM) with an empirical approach to consider the variation in the wetted surface and associated viscos effects. Some researchers also carried out CFD simulations. Guo *et al.* (2012) studied the contributions to the added resistance due to the ship motions at different wavelengths (λ) by simulating freely heaving, freely pitching and fixed models, and showed that the effect of motions on the added resistance is negligible for $\lambda/L_{WL} < 0.6$, where L_{WL} is the waterline length of ship. Sadat-Hosseini *et al.* (2013) investigated the effect of motions on the added resistance of a fixed and freely surging KVLCC2 model in short and long head waves. Shen *et al.* (2013) numerically investigated the added resistance and motion of DTMB5512 in head waves with a wide range of wave steepness. Shen *et al.* (2014) predicted the ship motion in irregular waves and compared their results with experimental data and the results from the strip theory. Sigmund *et al.* (2018) analyzed the effects of the ship speed, skin friction, wave steepness, ship type, as well as wave radiation and wave diffraction on the added resistance by both CFD and experiments for four ships in short and long regular head waves. Park et al (2019) discussed the tendency of added resistance in oblique sea conditions based on experimental data and numerical results for a ship model (S-VLCC) and observed the maximum value of the added resistance between the incident wave directions of $180°$ and $150°$. With focuses on the trimarans, Fang *et al.* (2008) investigated the wave loads on the trimaran with different side hull arrangements using spectral analysis and pulsating source potential method, in which the wave amplitude and the ship motion are assumed to be small to satisfy the linearity assumption. Min *et al.* (2011) applied a three-dimensional potential theory and the Green's function to optimize the trimaran by changing the layouts and length of the side hull to minimize the wave loads. Wu *et al.* (2011) studied the added resistance of a trimaran model in head waves using experimental data and CFD results. Sato *et al.* (2007) presented some results for the added resistance on two trimaran models with different longitudinal position of the side hulls subjected to head waves of difference lengths and small steepness, and indicated that the added resistance of the model with the side hulls at the central longitudinal position were smaller.

According to the publications available in public domain so far, as discussed above, the state of art on the study of the added resistance and seakeeping of trimarans can be summarized as below:

(1) The behaviors of the added resistance of trimarans have been studied under the conditions of head waves with small wave steepness in a few publications.

(2) Understanding on the added resistance of trimarans in oblique waves, particularly with strong nonlinearity, is very limited, if not at all.

(3) Although the seakeeping performance of trimarans has been more widely studied, the

correlation between the added resistance and motions of the ship is lack of systematic investigations, particularly subjected to oblique waves.

(4) Under the wave conditions with strong nonlinearity, the performance of trimarans should be stimulated by using CFD methods in nonlinear wave fields and considering wave breaking, water spray and intermittent emergence of side hulls. In literature, however, the implementation of CFD simulations is realized by specifying linear wave elevation and velocity at inlet boundary (the approach referred to as APP1 hereafter).

To gain better understanding on the performance of trimarans, this work makes effort in systematically investigate the properties of the added resistance of trimarans and its motions that mostly affect the added resistance. Various cases are considered, including these with different wave steepness, different wavelengths, different forward speeds and different incident wave angles.

The numerical approach adopted in this paper will be different from APP1. Our approach is to directly simulate trimarans moving in a large nonlinear wave field, rather than specifying conditions on inlet boundary. The approach will be referred to as APP2 hereafter. The situation modeled by APP2 is closer to the real situation of a ship in seaway compared with APP1. The approach will be realized by implementing the hybrid method, QaleFOAM, developed by Li *et al*. (2018) and Yan *et al.* (2019). A brief description on this method will be given in the next section.

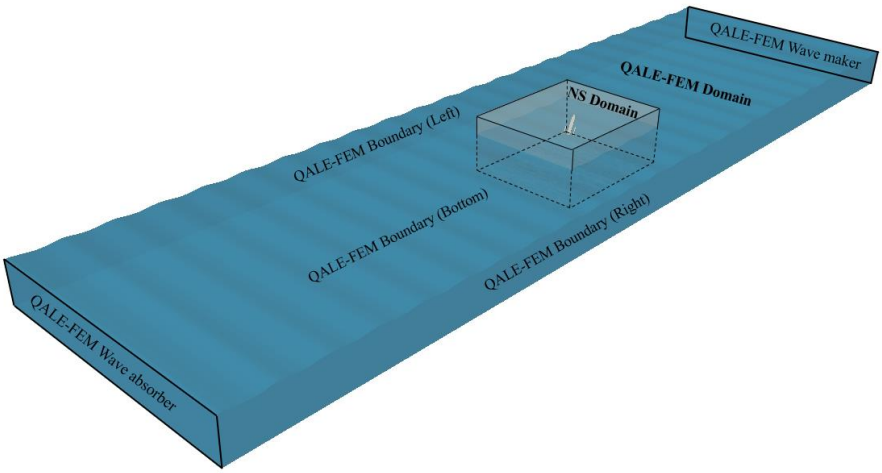

Fig. 1 Sketch of the computational domain for QaleFOAM

2 Mathematical models and numerical approaches

As indicated above, the problem associated with a trimaran moving in a wave field is numerically investigated by the QaleFOAM. The method couples the OpenFOAM based on the two-phase incompressible unsteady Navier-Stokes equations (named as NS model) with the QALE-

FEM based on the fully nonlinear potential theory (named as QALE-FEM model) using a zonal approach. As illustrated Fig. 1, the wave field covering a large domain (QALE-FEM domain) is simulated by the QALE-FEM while the small domain (NS domain) around the ship is dealt with by the OpenFOAM. The NS domain moves in the QALE-FEM domain at the forward speed of ships. Coupling interfaces with a relaxation zone between two domains are defined and moving to conform to the motion of the NS domain. The wave generated in the QALE-FEM domain is simultaneously transited into the NS domain through the coupling interfaces.

2.1 Mathematical model and formulation

The inertial coordinate system ($oxyz$) is used with its origin at the mean free surface with z-axis pointing upward and x-axis pointing to the wavemaker. In the QALE-FEM model, the flow is assumed to be incompressible, inviscid and irrotational. The governing equation and the associated boundary conditions are written in terms of the velocity potential ϕ (Ma *et al.*, 2015) as:

$$\nabla^2\phi = 0 \qquad \text{in the fluid domain} \tag{1}$$

$$\frac{\partial \phi}{\partial n} = \boldsymbol{n}.\boldsymbol{U} \qquad \text{on the wavemaker} \tag{2a}$$

$$\frac{\partial \phi}{\partial n} = 0 \qquad \text{on the right, left and bottom} \tag{2b}$$

$$\frac{\partial \boldsymbol{r}}{\partial n} = \boldsymbol{\nabla}\phi \qquad \frac{D\phi}{Dt} = -gz + \frac{1}{2}|\nabla\phi|^2 \qquad \text{on the free surface} \tag{3}$$

where $\boldsymbol{r}$ is the position vector of the free surface, $\boldsymbol{U}$ and $\boldsymbol{n}$ are the velocity and normal vector of the wavemaker boundary, t is time, D/Dt is the total time derivative, and g is the gravitational acceleration. On the wavemaker, the self-correction wave generation mechanism is employed to generate waves, while the localized self-adaptive wave absorber is applied on the wave absorber boundary to reduce the wave reflection (Yan *et al.*, 2017). As will being discussed in the following subsection, the trimarans are not included in the QALE-FEM domain and, thus, the boundary conditions on the trimaran surface are not needed.

In the NS model, the two-phase incompressible NS model is employed (Jasak, 2009) and summarized below for the corresponding ALE form (Wang *et al.*, 2013):

$$\frac{\partial(\rho u)}{\partial x} + \frac{\partial(\rho v)}{\partial y} + \frac{\partial(\rho w)}{\partial z} = 0 \tag{4}$$

$$\frac{\partial(\rho u)}{\partial t} + \nabla\cdot\left[\rho(u-u_g)\boldsymbol{U}_f\right] = \nabla\cdot\left(\mu\nabla u\right) - \frac{\partial p_d}{\partial x} + f_x \tag{5}$$

$$\frac{\partial(\rho v)}{\partial t}+\nabla\cdot\left[\rho(v-v_g)\boldsymbol{U}_f\right]=\nabla\cdot\left(\mu\nabla v\right)-\frac{\partial p_d}{\partial y}+f_y \tag{6}$$

$$\frac{\partial(\rho w)}{\partial t}+\nabla\cdot\left[\rho(w-w_g)\boldsymbol{U}_f\right]=\nabla\cdot\left(\mu\nabla w\right)-\frac{\partial p_d}{\partial z}+f_z \tag{7}$$

where ρ is fluid density, $\boldsymbol{U}_f=(u,v,w)$ is the fluid velocity and $\boldsymbol{U}_g=(u_g,v_g,w_g)$ is the velocity of the computational grid, p_d is the dynamic pressure, (f_x, f_y, f_z) represents external body force and , $f_z=-\rho g$ in this paper. The grid moves using the dynamic mesh technique (Xia *et al.*, 2012) to conform to the motion of the trimaran. The phase of the fluid is identified by the VOF (volume of fluid) method, in which ρ and μ are expressed by the volume fraction α as follows:

$$\rho=\rho_{water}\alpha+\rho_{air}(1-\alpha) \tag{8}$$

$$\mu=\mu_{water}\alpha+\mu_{air}(1-\alpha) \tag{9}$$

Where the volume fraction $\alpha=0$ represents the air while $\alpha=1$ represents the water, subscripts 'water' and 'air' denote the physical quantities of the water and air phases, respectively. Following the approach of Rusche (2002) and Weller (2002), the transportation of the volume fraction is governed by:

$$\frac{\partial\alpha}{\partial t}+\nabla\cdot\left[(\boldsymbol{U}_f-\boldsymbol{U}_g)\alpha\right]+\nabla\cdot\left[\boldsymbol{U}_r\alpha(1-\alpha)\right]=0 \tag{10}$$

where $\boldsymbol{U}_r=\min\left\{c_a\left|\boldsymbol{U}_f\right|,\max(\left|\boldsymbol{U}_f\right|)\right\}$ is the relative compression velocity and is used to compress the interface and is computed at the cell surface in the region of interface; $\boldsymbol{U}_f$ is the normal velocity at the cell surface. The compression coefficient c_α is set to unity here. All the governing equations are solved by the PISO (pressure-implicit split-operator) algorithm (Issa, 1986). More details about the equations of the NS model may be found from the documents and codes of OpenFOAM 3.0.

The laminar model is used in this paper for simulations. This is based on the evidence provided by Kim et al (2017), in which they compared the added resistance of S175 containership in oblique waves obtained by 3D potential method, CFD and experiments, and showed the difference between them was not very significant. Some numerical results obtained by the laminar model and turbulent model will be presented in Section 3.1 to demonstrate that the difference between them can be acceptable for the purpose of this paper.

The motions of ships in waves include the forward speed and oscillations induced by waves. The forward speed is constant and prescribed. The oscillated motions induced by waves are dynamically

solved in the NS model by the generic sixDoFRigidBodyMotion solver, which is based on the Newton's law for solving 6DOF (six-degree-of-freedom) motions of a rigid body (Xing *et al.*, 2008) and incorporated with the dynamic mesh technique available in OpenFOAM 3.0. In this paper, we are more interested in the added resistance and the motions which mostly affect it. According to Sprenger et al (2017), the force in oblique waves without forward speed obtained by 6 DOF and 3DoF (heave, roll and pitch) experiments can be quite similar. Park et al (2019) also showed some results for the added resistance at an incident wave angle of 120° obtained by restraining yaw, surge and sway, respectively, and suggested that the motions do not affect the added resistance significantly for the case they studied. On this basis, only heave, pitch and roll are considered in this paper with yaw, surge and sway being retained to make the simulations relatively easier. However, the effects of the retained motions, in particular the sway, should be taken into account if the motions are mainly concerned.

The force and moment due to fluid on the trimaran is estimated by integrating the pressure and viscous shear stress on the hull surfaces. The added resistance is calculated by the time-averaged total fluid force in the direction opposite the forward speed in waves minus total fluid force in the same direction in calm water at the same speed.

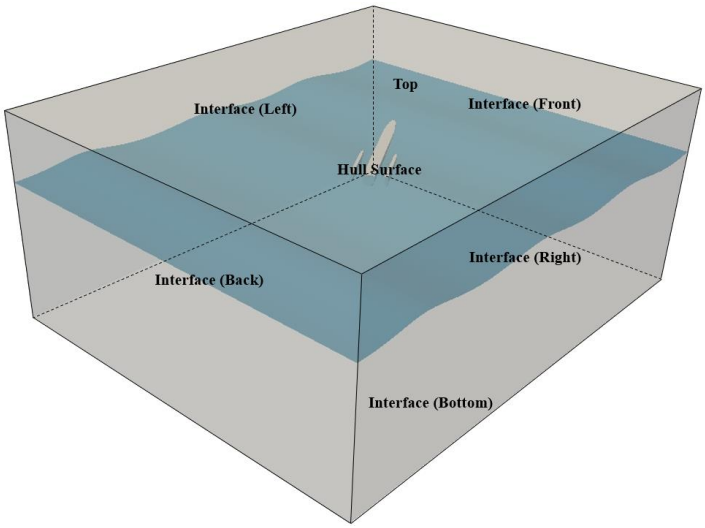

Fig. 2 Sketch of NS domain boundaries.

The boundaries of the NS domain are shown in Fig. 2. Except for the top boundary and hull surfaces, all the other boundaries of the NS domain are set as the interface, through which the OpenFOAM is coupled with the QALE-FEM, as described in the next subsection. The boundary conditions for the underwater part of the interface are assigned by the solutions from the QALE-FEM domain. In this paper, there is no wind, so the velocity for the above-water part of the interface is set to zero. This

may be acceptable for moderate speeds but may be cautious for the cases with very high speed. On the hull surface of ships, the nonslip condition is applied.

2.2 Coupling of two models

The coupling approach used in this paper is a one-way coupling, i.e., the OpenFOAM takes the solution of the QALE-FEM at the interface boundaries (Fig. 2) but does not feed its solutions back to the QALE-FEM, same as in Li *et al.* (2018) and Yan *et al.* (2019). To accommodate the coupling and the motion of the NS domain in the wave field, the QALE-FEM domain includes the space of the NS domain but without involving the trimaran, and the grid (described in the next subsection) for the water part in the NS domain is overlapped with the grid in the QALE-FEM domain.

To suppress the disturbed waves due to the trimaran propagating into the QALE-FEM domain, a relaxation zone (given in Fig. 6 in the next sub-section) is imposed in the NS domain and attached to the interface boundaries illustrated in Fig. 2. The wave is generated in the QALE-FEM domain and propagates into the NS domain through the interface boundaries and the relaxation zone, in which the velocity and the pressure are taken as a weighted summation of the solutions by the NS model and by the QALE-FEM. The weighting function ranges from 1 at the inner boundary of the relaxation zone to 0 at the outer boundary. The wave generation and propagation are demonstrated in Fig. 3. From the figure, one can see that, the wave generated in the QALE-FEM domain propagates into the NS domain, and, the wave field near the coupling boundaries are continuous and smooth, suggesting a satisfactory suppression of the disturbed wave due to the trimaran.

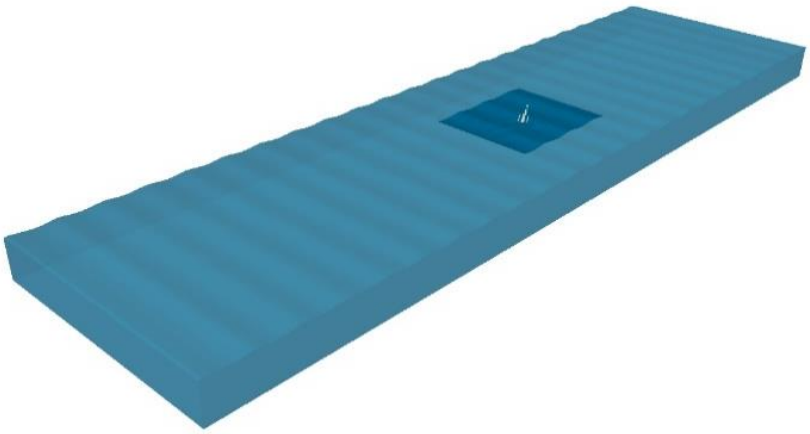

Fig. 3 Illustration of wave generation and propagation in the QaleFOAM (darker zone: water part of the NS domain)

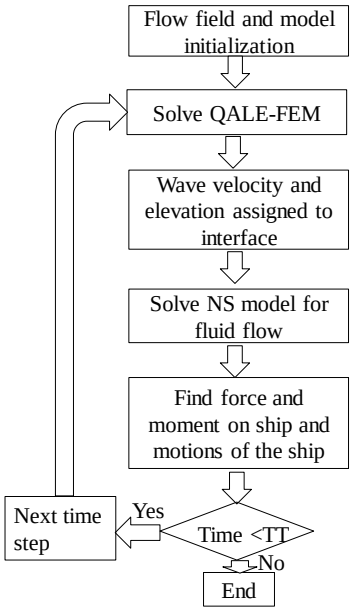

Fig. 4 Flow chart of the QaleFOAM (TT: total time duration to be simulated).

In the implementation of the QaleFOAM, the grid used by the QALE-FEM and that by the OpenFOAM are different. In addition, the time step used for the QALE-FEM can be much larger than that used by the NS model based on our previous publications (e.g. Ma *et al.,* 2009; Li *et al.,* 2018). The differences can be effectively handled by the spatial-temporal interpolation scheme suggested by Yan *et al*. (2019) for the floating body without a forward speed. However, a distinguishing challenge in this paper from previous publications (Li *et al.* 2018; Yan *et al*., 2019) is that the NS domain moves in the QALE-FEM domain at the forward speed of the trimaran, and thus the interface boundaries and associated relaxation zones are moving during the simulation. This brings more difficulties on the temporal interpolation. Due to this reason, the QALE-FEM model is set to use the same time step as the NS model in the QaleFOAM implementation here. It is fortunate that the computational time of the QALE-FEM model is just a small fraction of the computational time taken by the NS model, and so the smaller size of time step purposely chosen for the QALE-FEM model does not significantly slow down the whole simulation process. The flow chart of the QaleFOAM is illustrated in Fig. 4.

2.3 Computational domain and meshing of QaleFOAM

The sizes of the computational domain are determined by numerical tests. The details of the tests are not given for limiting the length of the paper but the appropriateness of the chosen sizes is demonstrated by the validations presented in the next section. Based on the tests, the length and depth of the QALE-FEM domain is $40L_{WL}$ and $2L_{WL}$ (L_{WL} is the waterline length of the trimaran),

respectively. The width of the domain can be arbitrary as only the unidirectional incoming wave field are simulated, though it would have different incident angles relative to the trimaran, which is achieved by adjusting the moving direction of the NS domain.

The NS domain is defined by the two boxes as shown in Fig. 5. The vertical surfaces of the inner box are the inner boundaries of the relaxation zone and the vertical surfaces of the outer box are the outer boundaries of the relaxation zone, which are the interface boundaries of the NS domain shown in Fig. 2. The vertical surface of the inner box before the foremost of the trimaran is $1.0L_{WL}$ while it is $1.5L_{WL}$ behind the stern. The side vertical surfaces of the inner box are set as $1.2L_{WL}$ from the ship. In the vertical direction, the NS domain extends from under the calm water surface to $0.5L_{WL}$ above the calm water surface. The distance between the inner and outer boxes are 0.3λ at the inlet, 0.6λ at outlet and 0.2λ on both sides, where λ is the wavelength.

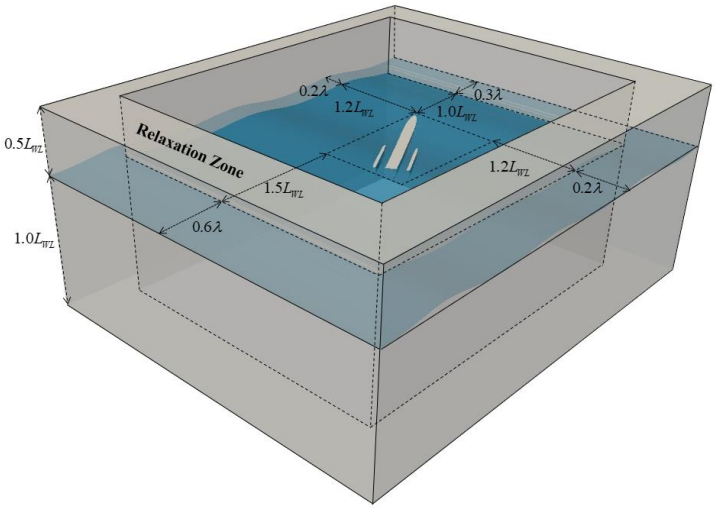

Fig. 5 Sketch of the NS domain size and relaxation zone.

(a)

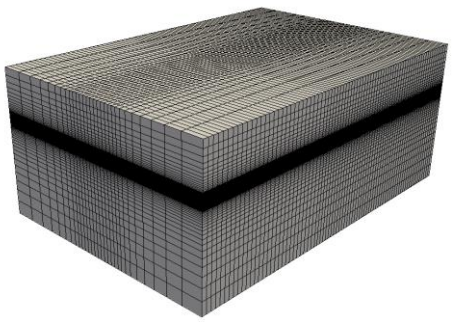

(b)

(c) (d)

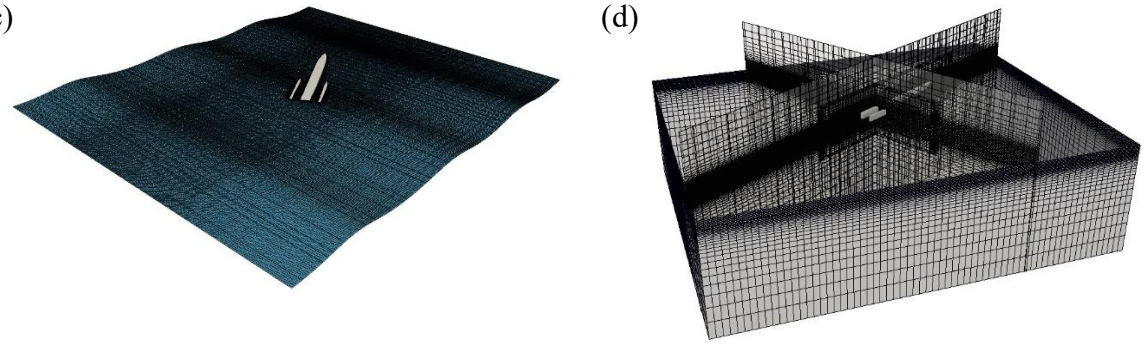

Fig. 6 Sketch of mesh of domain and hull surface. (a) NS domain, (b) hull surface, (c) free surface and (d) near the ship.

The grid in the NS domain is generated by the snappyHexMesh in OpenFOAM. The basic idea is to use the closed surface to trim the portion of the background grid occupied by the trimaran, resulting in a computational grid for the fluids. This is necessarily followed by the local adjustment/re-construction of the cells near the closed surface to improve the grid quality. The background grid is generated first using the blockMesh. To ensure a sufficient grid resolution near the water surface and the trimaran hull, the background grid is hierarchically refined in these regions, as illustrated in Fig. 6(a). Furthermore, it is well-known that the resolution and the quality of the cells near the structure surface play a critical role for WSI problems. For this reason, several layers of body-fitted cells are added on the surface of the trimaran using the snappyHexMesh tool. The computational grid near the free surface and the trimaran surface are illustrated in Fig. 6(c) and (d), respectively.

3 Verification and Validation

Although the accuracy, reliability and efficiency of the QaleFOAM has been demonstrated by Ransley *et al.* (2019) for modelling a fixed offshore structure, it will be further validated by comparing its results with experimental data for a trimaran model in this section. Before the validation, the convergent behaviors of the QaleFOAM will be first discussed below.

3.1 Tests on grid convergence and the effects of turbulence

Before the seakeeping performance and the added resistance of trimaran is investigated, the tests on grid convergence are carried out firstly. Because the tests about the wave generation by QALE-FEM has been well documented (for example, Ma *et al.*, 2009; Li *et al.*, 2018), only the tests of the grid in the NS domain are carried out in this paper. For this purpose, a trimaran model named as TRI1 is used. The main characteristic dimensions of its center hull are $B_{WL}/L_{WL} = 0.08$, $D_{WL}/L_{WL} = 0.04$, $C_b = 0.52$, while these for the side hulls are $B_{WL1}/L_{WL1} = 0.05$, $D_{WL1}/L_{WL1} = 0.04$, $C_{b1} =$

0.46. The gravity center of TRI1 is at $x_g/L_{WL} = -0.15$, $y_g/L_{WL} = 0$, $z_g/L_{WL} = 0.02$, and the side hull position is at $d_1/L_{WL} = 0.1$, $d_2/L_{WL} = 0$, where d_1 is the distance between the center hull and side hull, and d_2 is the longitudinal distance between the center hull stern and the side hull stern. The sketch of trimaran model is shown as in Fig. 7.

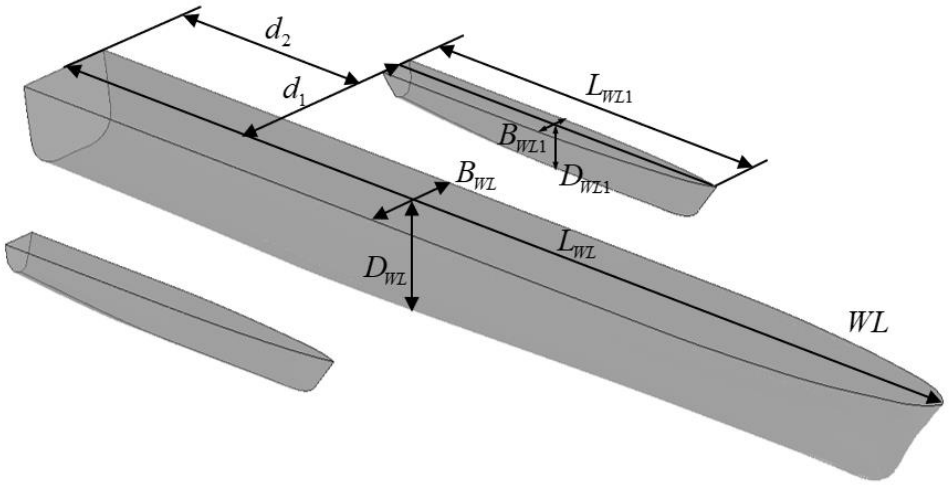

Fig. 7 The sketch and main characteristic dimensions of trimaran (TRI1).

The wave with the length ratio of $\lambda/L_{WL} = 1.09$ and the steepness of $ak = 0.135$ is employed for convergence tests, and the cases with the ship moving in both head wave ($\beta = 180°$) and oblique wave ($\beta = 135°$) are simulated. The TRI1 model is advancing at $Fr = 0.353$. Three sets of mesh are used for the simulations, which is summarized in Table 3. Based on the reference (Kim *et al.*, 2017), the mesh is refined by reducing the cell sizes through changing the number of $\lambda/\Delta x$ in the horizontal direction and $H_W/\Delta z$ (H_W is the wave height) in the vertical direction when the mesh is generated. The corresponding cell numbers of the Fine (G_1), Medium (G_2) and Coarse (G_3) meshes are 4.06×10^6, 1.45×10^6 and 0.51×10^6 for cases with $\beta = 180°$, and 4.51×10^6, 1.61×10^6 and 0.59×10^6 for cases with $\beta = 135°$, respectively.

Table 3

Grids for convergence tests on TRI1

Grid name	Hull form	Mesh	$\lambda/\Delta x$	$H_w/\Delta z$	T_e/dt
G_1		Fine	112	11	364
G_2	TRI1	Medium	80	8	260
G_3		Coarse	55	5	185

The results for the cases will also be used to perform the error and uncertainty analysis using the

procedure recommended by ITTC (2017). For this purpose, the grid refinement ratio is kept at a constant with $r_G = \sqrt{2}$ as shown in Table 4, in which the first order Richardson extrapolation δ^*_{REG4}, accuracy order p_G, correction factor C_G and grid uncertainty U_G are calculated by:

$$R_G = \frac{\varepsilon_{G21}}{\varepsilon_{G32}} \tag{12}$$

$$p_G = \frac{ln[(\varepsilon_{G32})/(\varepsilon_{G21})]}{ln\, r_G} \tag{13}$$

$$\delta^*_{REG} = \left(\frac{\varepsilon_{G21}}{r_G^{p_G}-1}\right) \tag{14}$$

$$C_G = \frac{r_G^{p_G}-1}{r_G^{p_{G_{est}}}-1} \tag{15}$$

$$U_G = |C_G \delta^*_{REG}| + |(1-C_G)\delta^*_{REG}| \tag{16}$$

where $p_{G_{est}} = 2$ is used in Eq. (15), $\varepsilon_{Gij} = f_{G_i} - f_{G_j}$ is the difference between f_{G_i} and f_{G_j}, and f_{G_i} is the computed result by using Grid G_i.

Table 4

Results of error and uncertainty analysis (TRI1)

β		r_G	p_G	C_G	δ^*_{REG}	R_G	U_G	U_G/f_{G_1}
180°	$R_{aw}/(\rho g a^2 B_{WL}^2/L_{WL})$	$\sqrt{2}$	1.509	0.687	0.663	0.593	0.663	4.103%
	ξ_3/a		1.808	0.871	0.025	0.534	0.025	3.374%
	ξ_5/ak		-2.652	-0.601	0.000	2.507	0.001	0.141%
135°	$R_{aw}/(\rho g a^2 B_{WL}^2/L_{WL})$	$\sqrt{2}$	1.709	0.808	0.383	0.553	0.383	3.909%
	ξ_3/a		1.261	0.548	0.027	0.646	0.027	3.553%
	ξ_4/ak		7.306	11.579	0.000	0.079	0.006	1.389%
	ξ_5/ak		-0.695	-0.214	-0.011	1.272	0.016	2.114%

The test results of added resistance as well as the amplitudes of heave (ξ_3), roll (ξ_4) and pitch (ξ_5) are shown in Fig. 8 corresponding different grids employed. The amplitudes of motions are found by the formula of (peak point value - trough point value)/2, where the peak and trough point values are taken from the time histories of the steady part of motions. The figures indicate that the variation of results with the cell number is roughly monotonic for both $\beta = 180°$ and $\beta = 135°$. For both incident wave angles, the difference of results obtained by the medium and fine grids for the cases is acceptably small and so the medium (G_2) may be considered as suitable.

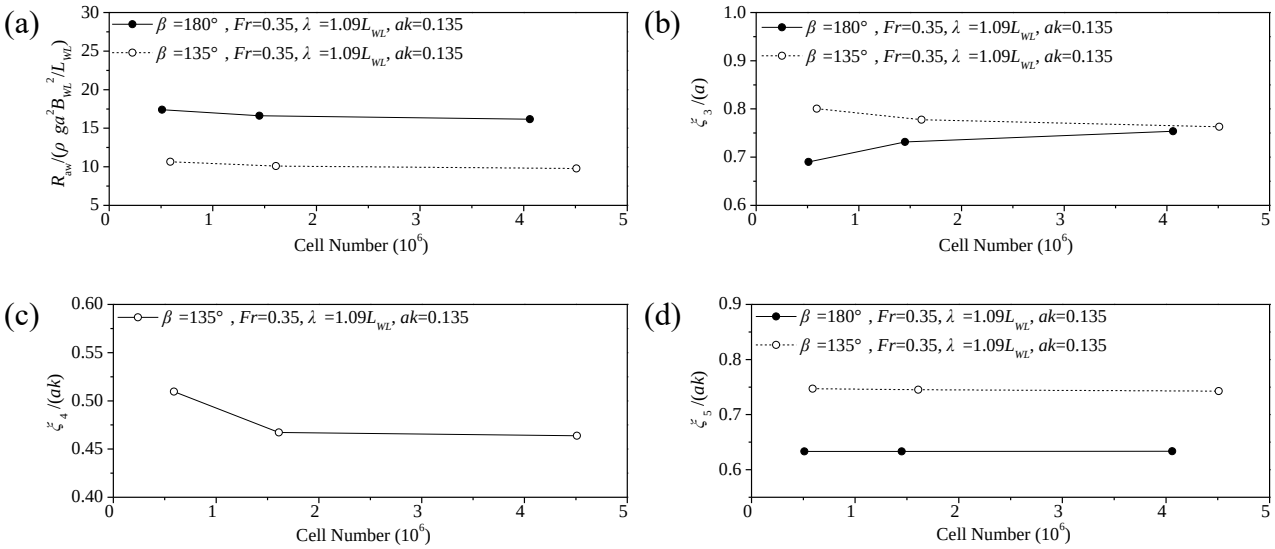

Fig. 8 Grid convergence tests. (a) added resistance, (b) heave, (c) roll, (d) pitch.

Table 4 outlines the error and results of the grid uncertainty analysis calculated by Eqs. (12)-(16). It can be seen that in all the cases, the values of C_G are significantly different from 1, which justify the use of these equations for estimating the error and uncertainty of the numerical results recommended by ITTC (2017). From the table, one can find that the uncertainty of all the cases is near or less than 4.2%, which is considered as acceptable. It is noted that the values of R_G for pitch are large than 1. That is because the pitch amplitudes from three sets of data are very close to each other and their differences are almost invisible (Fig. 8d), indicating that the results for pitch have indeed converged.

As indicated before, the laminar model is applied in this paper in the NS domain of QaleFOAM. To show the effects of turbulence, a few cases are run by using the laminar model and the kOmegaSST turbulent model. The cases include these of the TRI1 in heading wave ($\beta = 180°$, $ak = 0.061$, $\lambda/L_{WL} = 1.38$) and oblique wave ($\beta = 135°$, $ak = 0.135$, $\lambda/L_{WL} = 1.09$) at $Fr = 0.35$ by using the fine mesh (G_1). The computed results are compared in Fig. 9 and Fig. 10.

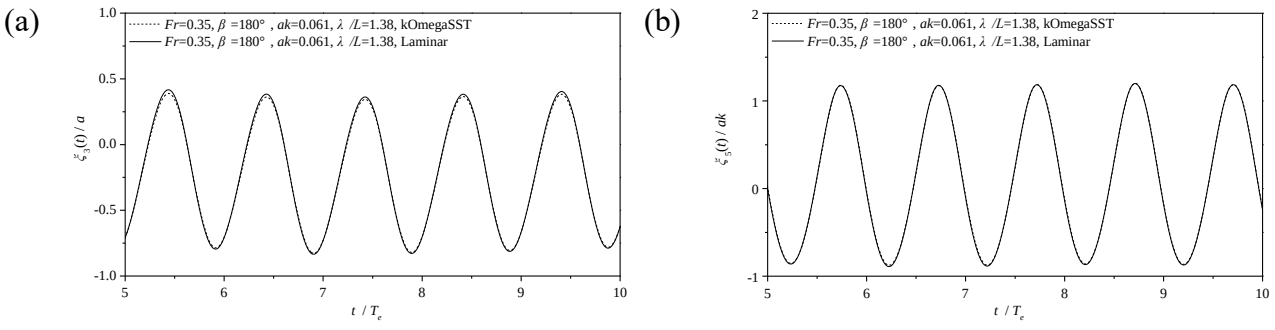

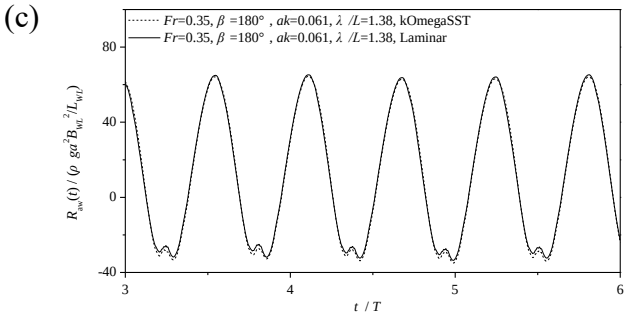

Fig. 9 Compute results for TRI1 by laminar and K-omega SST models ($Fr = 0.35,\ \beta = 180°,\ ak = 0.061,\ \lambda/L_{WL} = 1.38$)

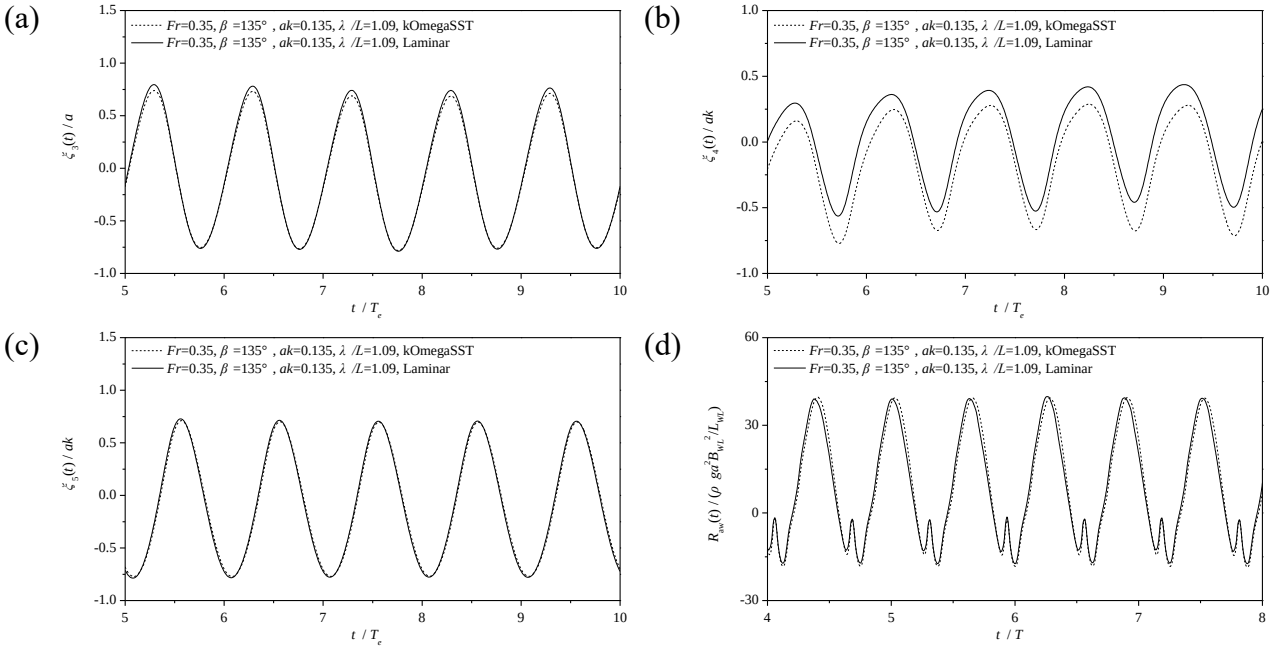

Fig. 10 Compute results for TRI1 by laminar and K-omega SST models ($Fr = 0.35,\ \beta = 135°,\ ak = 0.135,\ \lambda/L_{WL} = 1.09$)

For the case in the heading wave, it is seen, from Fig. 9, that the effects of the turbulent model are almost invisible. For the case in the oblique heading wave, as shown in Fig. 10, the effects of the turbulence model on the added resistance and the motions of heave and pitch are still not much noticeable. However, the time history of roll motions obtained by kOmegaSST model is obviously different from that by the laminar model. Nevertheless, the motion presented in this paper is its amplitude computed by (peak point value - trough point value)/2 as indicated before. The difference in the amplitudes computed in this way is less than 1.5% for the roll motions obtained by the laminar and turbulent models. These facts evidence that the results from the laminar model are acceptable for the purpose of this paper. However, if one is more interested in the details of the motions, the proper turbulent model may have to be used.

3.2 Comparison of numerical and experimental results

To validate the current method, the experiment on TRI1 was carried out in the towing tank of the Harbin Engineering University (HEU), which is 110m length, 7m width and 3.5m depth. The waves with different wavelengths and steepness are generated by a hydraulically driven wavemaker. The model is illustrated in Fig. 11. The center hull and side hulls are rigidly connected by two transverse connecting bars. The ship model is towed against the incident waves. The motions of the model in waves are measured by a 4-DoF instrument, which is fixed to the gravity center of the hull, and a tail rod is used to control the moving direction of the model. The test conditions of TRI1 for both model experiment and numerical simulation are listed in Table 5.

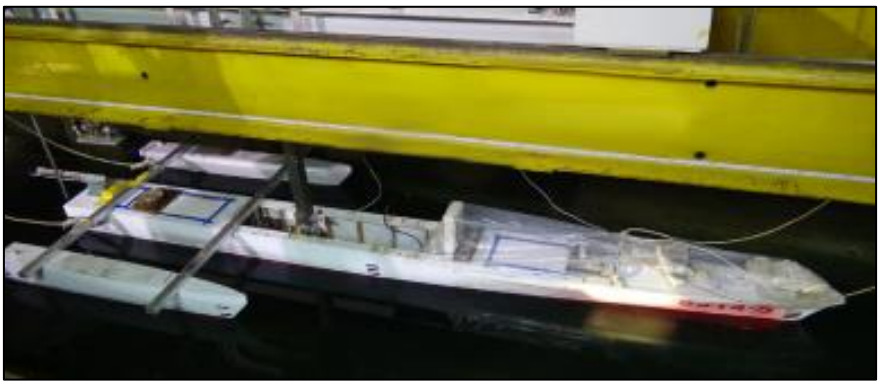

Fig. 11 TRI1 model in head waves.

Table 5

Operating conditions of TRI1 model for validation in head seas.

Case name	Hull form	Fr	λ/L_{WL}	ak	ω_e
C10	TRI1	0.35	no incident wave		
C11			0.73	0.065	9.19
C12			0.88	0.065	8.05
C13			1.09	0.062	6.94
C14			1.38	0.061	5.91
C15			1.50	0.063	5.59
C16			1.80	0.058	4.95
C17			2.25	0.047	4.28

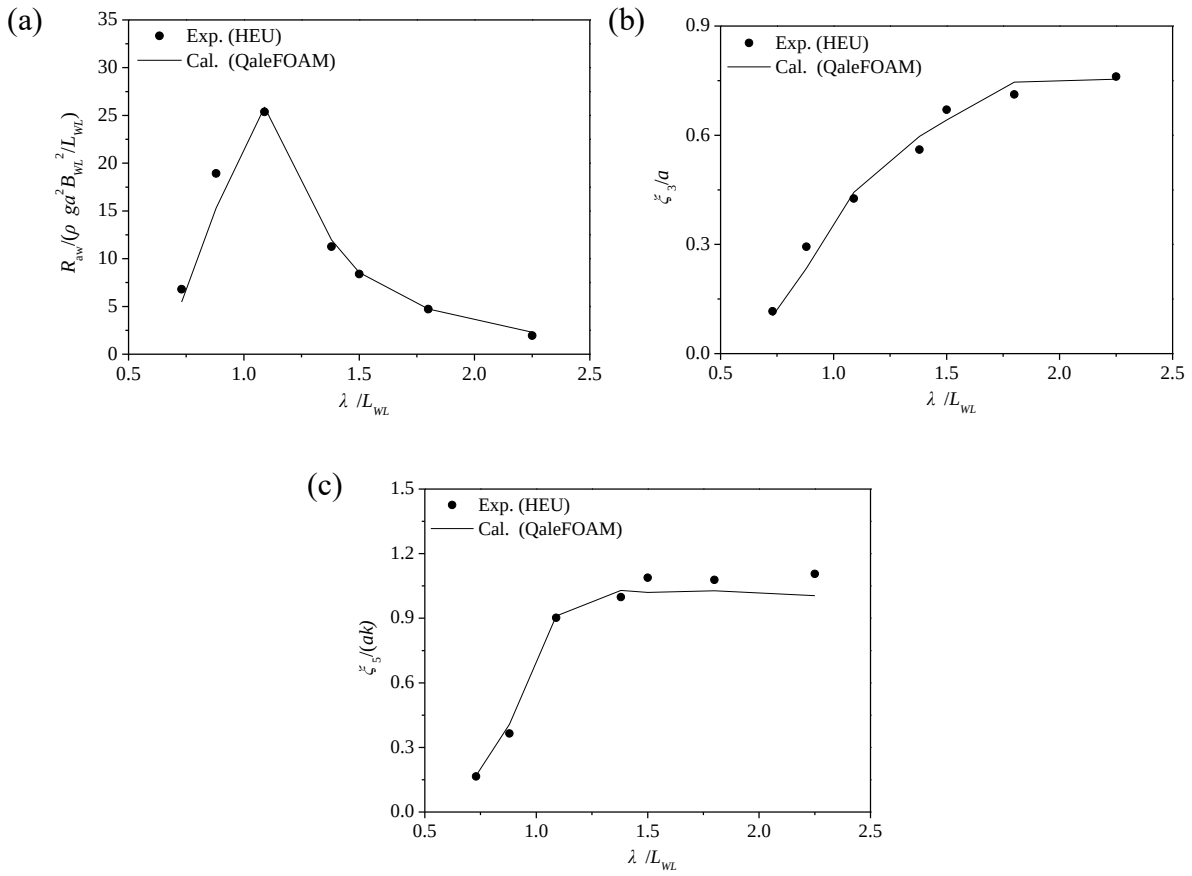

Fig. 12 Numerical and experimental results of TRI1 model. (a) added resistance, (b) heave, (c) pitch.

The medium mesh scheme and time step are used for the numerical simulations, as concluded in Section 3.1. The towing tank experiment and numerical simulation of the cases with and without incident wave are both carried out. The numerical results of added resistance, heave and pitch are compared with the experimental results in Fig. 12. The figure shows that the numerical results, denoted by Cal. (QaleFOAM), are in quite good agreement with the experimental results in all the cases considered. The main difference of the added resistance appears at the cases with small wavelength where the computed added resistance is slightly smaller than the experimental ones. The largest difference of motion responses appears at the pitch motion with the larger than $\lambda/L_{WL} = 1.38$, where the simulations underestimates the pitch motion but the largest difference is about 10%.

4 Investigation on different approaches of simulating ships advancing in waves

As indicated in the Introduction, the commonly used approach for simulating a ship advancing in waves is the APP1 approach (e.g. Orihara *et al.*, 2003; Sadathosseini *et al.*, 2013; Simonsen *et al.*, 2013; Shen *et al.*, 2014), in which the ship is kept without forward speed while the uniform current

with the same magnitude but in an opposite direction of the ship velocity are assigned at the inlet boundary together with the incident waves. The approach adopted in this paper is the APP2, different from APP1 employed in the literature, that directly simulates the ships advancing in the wave field, more similar to real scenarios. Compared with the APP1, the APP2 needs a larger computational domain to simulate the wave field. The question is whether the two approaches would give the same results. To answer this question, some results are presented in this section, obtained by the two approaches for a number of cases with different values of wave steepness, as listed in Table 6. One can see from the table that in all these cases, the Froude number corresponding to the forward speed or current is 0.35. Two values of the wave steepness are considered, one is 0.058 and the other is 0.135. In Table 6, ω and ω_e are the circular frequency of incident wave for APP2 (C18 and C19) and the encountering circular frequency of incident wave for APP1 (C20 and C21), respectively. The incident waves for C20 and C21 are assigned using the linear wave theory at the inlet of the domain. The computation domain for C20 and C21 is the same as shown in Fig. 5.

Table 6

Parameters for investigating different approaches (head sea).

Case	Hull form	λ/L_{WL}	ak	ω	ω_e	$U_{ship}/\sqrt{gL_{WL}}$	$U_{current}/\sqrt{gL_{WL}}$
C18	TRI1	1.09	0.058	4.339	-	0.35	-
C19	TRI1	1.09	0.135	4.339	-	0.35	-
C20	TRI1	1.09	0.058	-	8.017	-	0.35
C21	TRI1	1.09	0.135	-	8.017	-	0.35

(a)

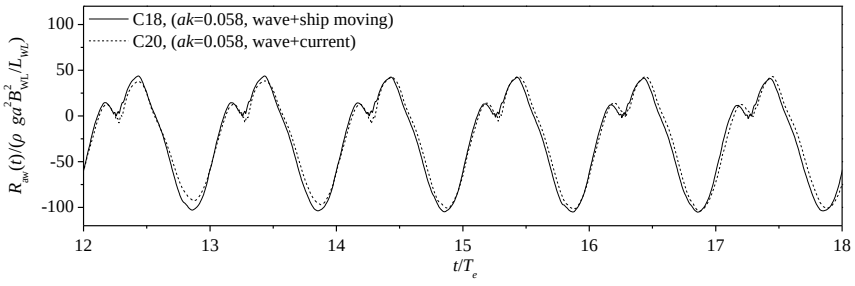

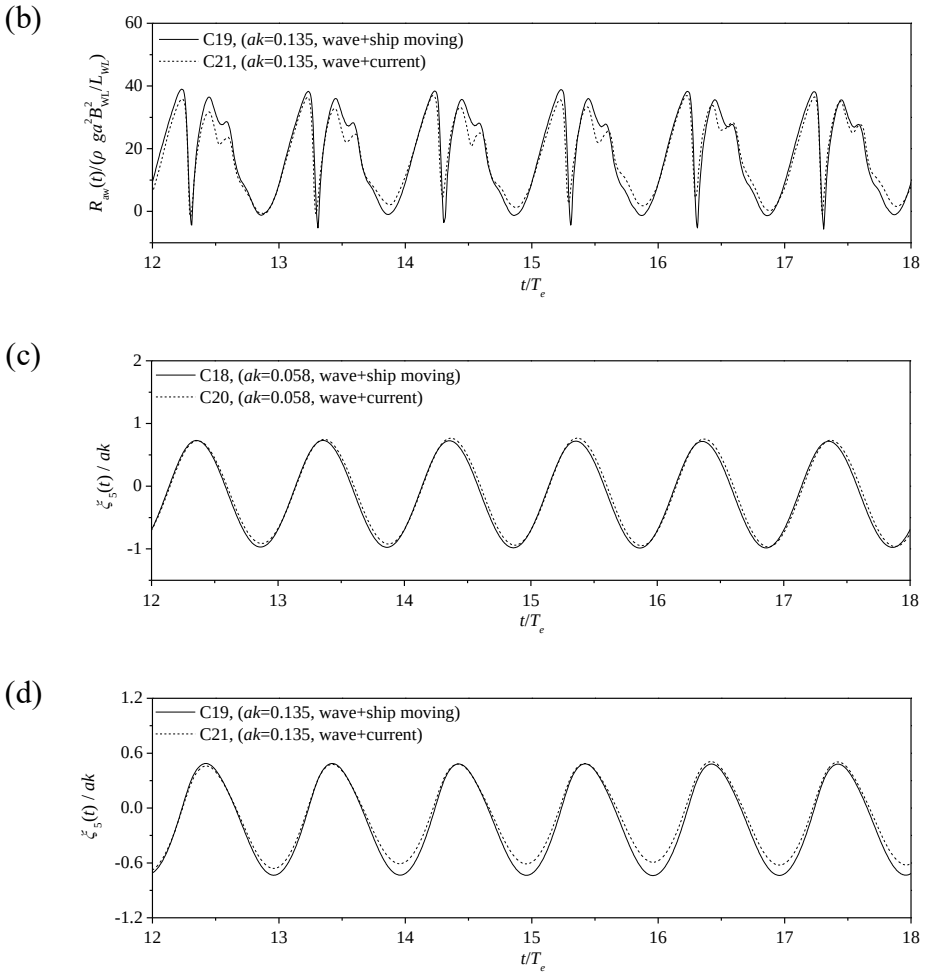

Fig. 13 Comparison of numerical results by two approaches, (a) total resistance in wave with $ak = 0.058$, (b) total resistance in wave with $ak = 0.135$, (c) pitch motion in wave with $ak = 0.058$, (d) pitch motion in wave with $ak = 0.135$.

The time histories for non-dimensional resistance in waves and pitch motion after becoming steady are plotted in Fig. 13. From this figure, it can be seen that the computed results obtained by the two approaches are almost the same when the wave steepness is small ($ak = 0.058$, Fig. 13(a) and (c)). When the wave steepness is as large as $ak = 0.135$, however, the largest difference between the results obtained by the approaches shown in Fig. 13(b) and Fig. 13(d) could be as large as 18% and 17%, respectively. The differences may be due to the following reasons. One is that the forward speed in APP2 or in real cases does not directly affect the wave properties while the current representing the forward speed and input at inlet in APP1can directly interact with the incident waves, which can be significant when the wave steepness is large enough. The second reason is that the incident waves assigned at the inlet in the APP2 approach are calculated by the fully nonlinear while they are specified by using the linear wave theory in APP1. Nevertheless, the difference caused by the second reason may not be significant as the linear theory is considered as accurate enough for evaluating the wave kinematics at such a steepness. Based on these results, APP2 would be preferred

unless it is known that the significance of wave-current interaction is negligible. Implementing the APP2 requires the much larger computational domain and so the numerical method must be computationally efficient enough. The QaleFOAM meets such requirement and so can be used for the APP2. It is noted that there is some suspicion on the effect of the interaction between the incident waves and the current representing the forward speed in the APP1 (Nowruzi, et al, 2020a) but no quantitative information about the effect, as shown in Fig. 13, has been given in literature so far.

5 Results and discussions

In this section, the cases for another ship, named as TRI2, moving in different waves will be discussed. The effects of wave conditions and forward speeds on the added resistance and motions are discussed. The mesh similar to the medium scheme (G_2) and the time step as shown in Table 3 are used for all the numerical simulations below.

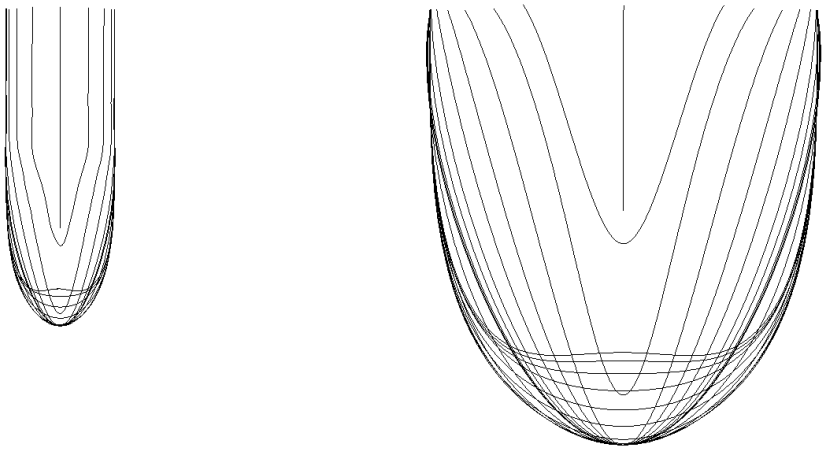

Fig. 14 Section lines of TRI2 model. (a) left: side hull, (b) right: center hull.

The hull form of TRI2 is similar to TRI1, but the block coefficients of both the center hull and the side hulls of TRI2 is slightly larger than that of TRI1. The section lines of TRI2 are shown in Fig. 14. The main characteristic dimensions of TRI2 are $B_{WL}/L_{WL} = 0.08$, $D_{WL}/L_{WL} = 0.04$, $C_b = 0.56$ $B_{WL1}/L_{WL1} = 0.05$, $D_{WL1}/L_{WL1} = 0.04$, $C_{b1} = 0.54$. The gravity center of TRI2 is at $x_g/L_{WL} = -0.13$, $y_g/L_{WL} = 0$, $z_g/L_{WL} = 0.024$, and the side hull position is at $d_1/L_{WL} = 0.12$, $d_2/L_{WL} = 0$.

5.1 Effects of wave steepness

For the cases in this section, the TRI2 is moving forward at $Fr = 0.35$ (corresponding to the design speed) in waves under different wave steepness and wave directions with the wavelength being$\lambda/L_{WL} = 1.09$, as given in Table 7. The reason for selecting this value of the wavelength is because of the maximum added resistance occurs near this value as seen in Fig. 12. The results for other forward speeds will be presented in later sections.

Table 7

Parameters for TRI2 moving in waves with different steepness and directions.

Hull form	Fr	λ/L_{WL}	ak	β (deg)
TRI2	0.35	1.09	0.058 0.096 0.135	180, 165, 150, 135, 120, 105, 90

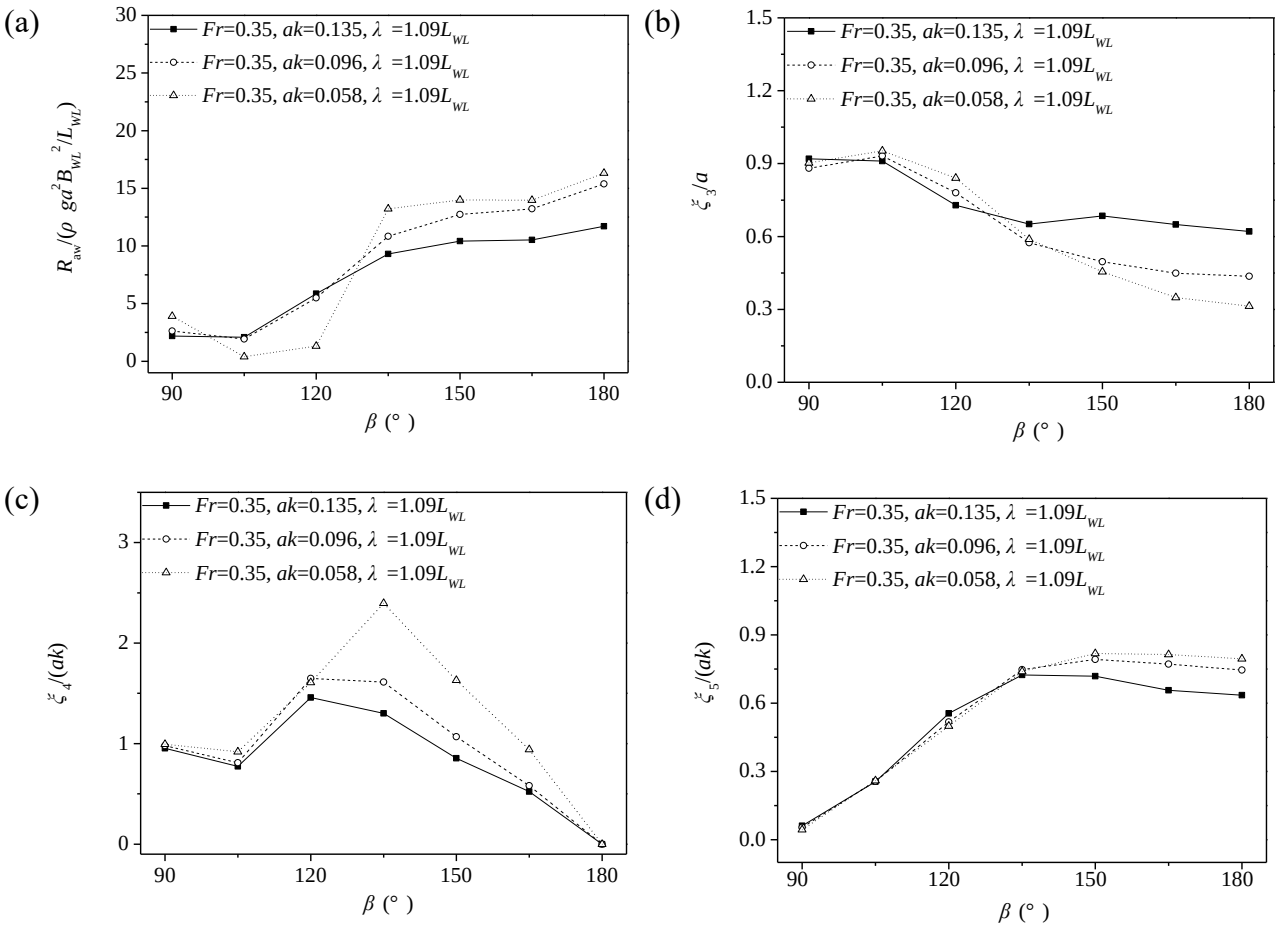

Fig. 15 Computed results for TRI2 moving in waves with different steepness and directions (a) added resistance, (b) heave amplitudes, (c) roll amplitudes, (d) pitch amplitudes.

The nondimensionalized computed results of the added resistance and motions are shown in Fig. 15. As can be seen, the effects of wave steepness on the computed result is more significant when incident wave angle β is larger than $120°$. For example, the difference in the nondimensionalized added resistance for $ak = 0.058$ and $ak = 0.135$ is about 30% when $\beta \geq 135°$. With the change of incident wave angles, the added resistance and motions vary dramatically but in different ways. The added resistance and pitch motion become larger with the increase of incident wave angles until about $135°$. After it, their variations are insignificant. The trend of the heave motion is different: its largest values occurring near the beam sea and decreasing when the ships moving toward to the head sea. When the incident angle is larger than $120°$, the nondimensionalized heave increases with the increase of wave steepness. The roll motion is an important parameters of seakeeping performance in the oblique waves. It is interesting to see from Fig. 15(c) that the peak value of roll motion appears around $\beta = 135°$, not at the beam sea, which is different from traditional mono-hull as indicated by Mizoguchi *et al.* (1981), for which the peak roll motion amplitude of mono-hull usually appears at the beam sea ($\beta \geq 90°$). Another point worth discussing is that the added resistance, pitch, heave and roll are less sensitive to the wave steepness when the wave incident angle is near $90°$ (beam sea).

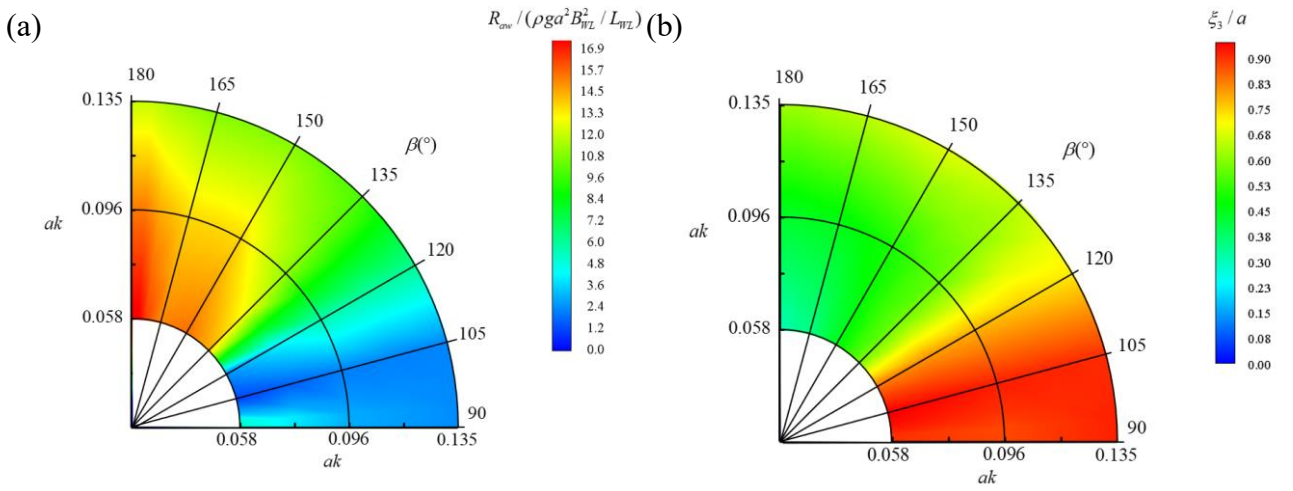

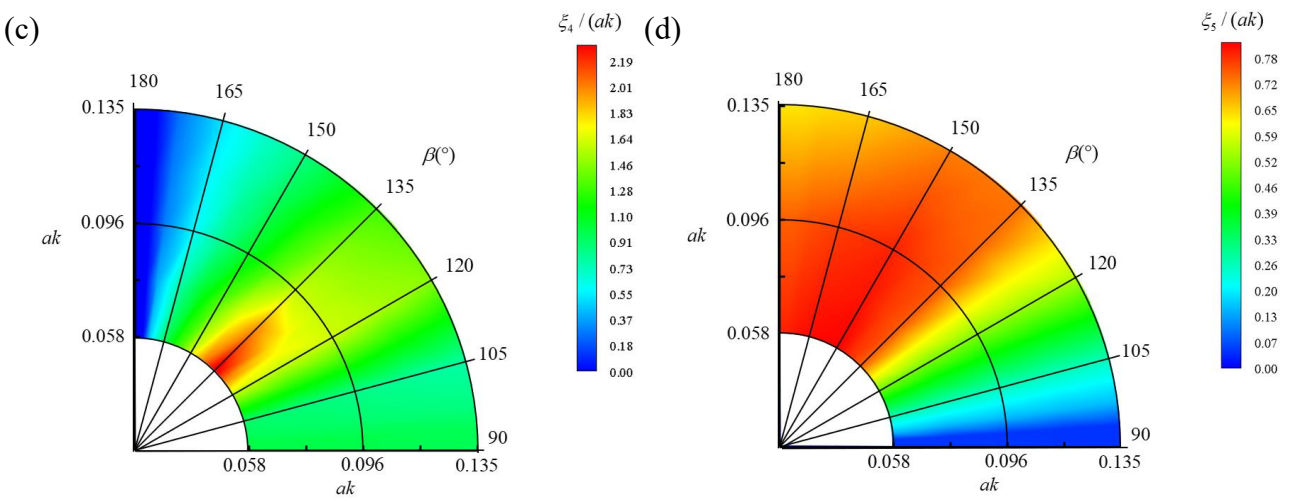

Fig. 16 The added resistance and motion amplitudes of TRI2 in waves with different steepness and directions ($\lambda/L_{WL} = 1.09$): (a) added resistance, (b) heave, (c) roll, (d) pitch.

Fig. 16 shows the variation of added resistance and motion response of TRI2 with both wave steepness and wave directions in another way. They clearly illustrate the features already discussed about Fig. 15. In addition, they also illustrate the areas in which some quantities are significant or insignificant. As observed from Fig. 16(a) and (c), the areas with significant values of nondimensionalized added resistance and pitch motions both lie in the region between $0.058 < ak < 0.135$ and $120° < \beta < 180°$ but their size and shape are very different. The area for significant nondimensionalized added resistance is quite smaller and irregular but that for pitch motion is quite larger and regular. The area for significant nondimensionalized roll values is only limited within a small region around the point $ak = 0.058$ and $\beta = 135°$.

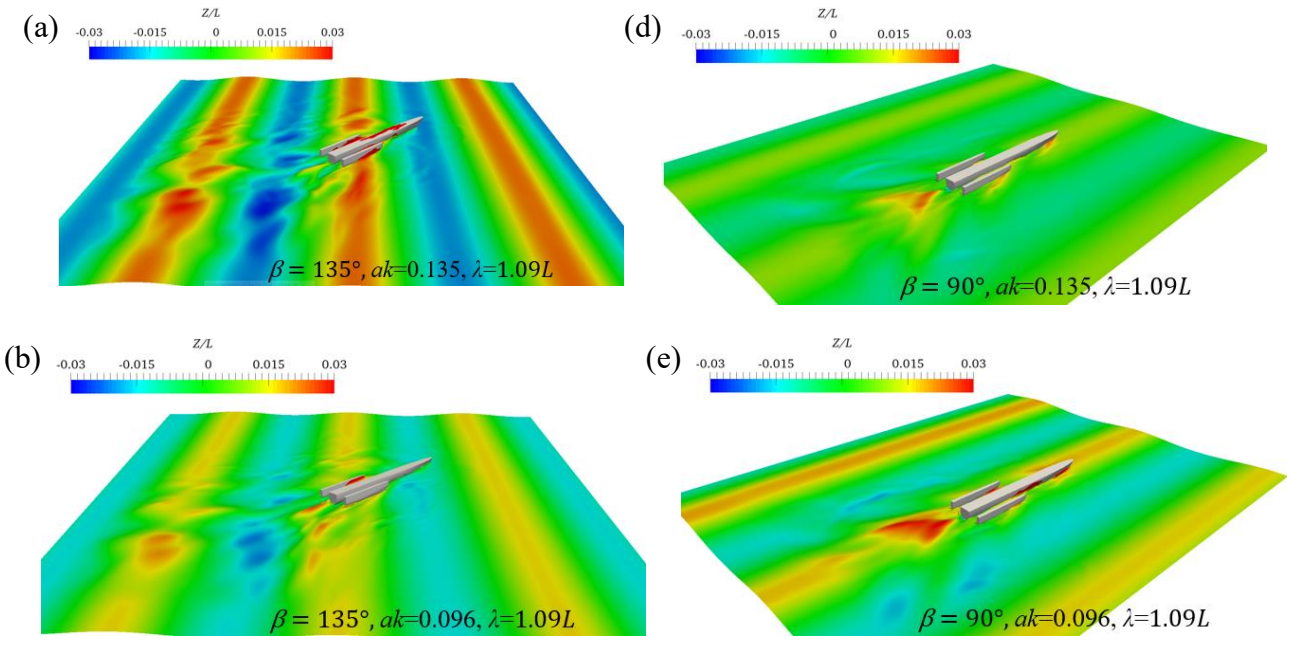

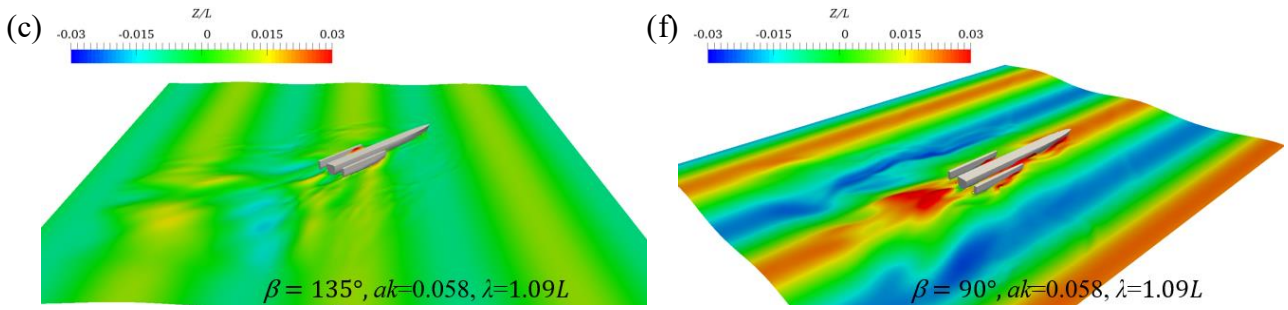

Fig. 17 Snapshots of the free surface around TRI2 with $\lambda = 1.09L_{WL}$: (a) $ak = 0.135$, $\beta = 135°$, (b) $ak = 0.096$, $\beta = 135°$, (c) $ak = 0.058$, $\beta = 135°$, (d) $ak = 0.135$, $\beta = 90°$, (e) $ak = 0.096$, $\beta = 90°$, (f) $ak = 0.058$, $\beta = 90°$.

Fig. 17 presents the snapshots of the free surface around TRI2 for some cases in Fig. 15-Fig. 16, which are captured when the peak of incident wave passes the center of the main hull. It shows that the surface elevation between the left side hull and center hull is much larger than that between the right side hull and the center hull (Fig. 17(a), (b), (c)) for the wave incident angle of $\beta = 135°$. Such difference in the cases of $\beta = 90°$ is not so noticeable. This is perhaps the reason why the roll at $\beta = 135°$ is larger than that at $\beta = 90°$. It also shows that green water on deck occurs in the case of $\beta = 135°$ and $ak = 0.135$, but not in the case of $\beta = 90°$ and $ak = 0.058$. This may be considered as an explanation that the nondimensionalized heave for the former is larger than that for the latter as observed in Fig. 15(b)

In addition, the degree of asymmetry of disturbed wave patterns about longitudinal plane of the main hull becomes higher with the increase of wave steepness for $\beta = 135°$ as observed in Fig. 17(a), (b) and (c) while the change of asymmetrical degree is not significant for $\beta = 90°$ as seen in Fig. 17 (d), (e) and (f). This may explain, at least partially, why the added resistance, pitch, heave and roll are more sensitive to the wave steepness for the cases when the wave incident angle is larger than the cases with the wave incident angle being near $90°$.

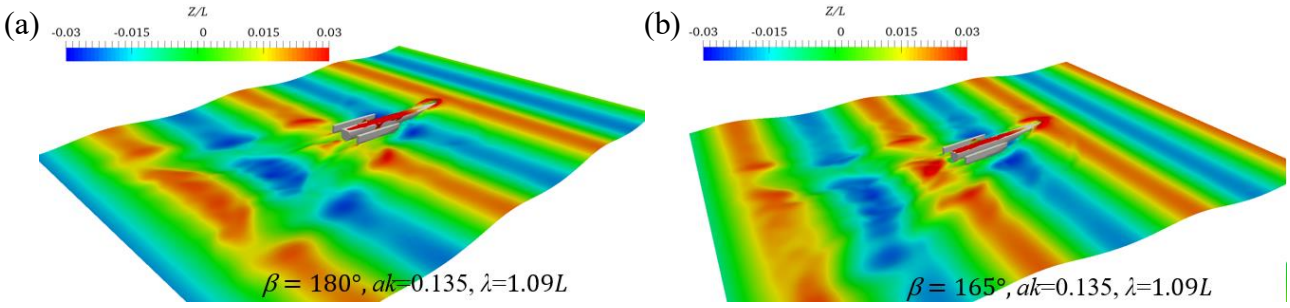

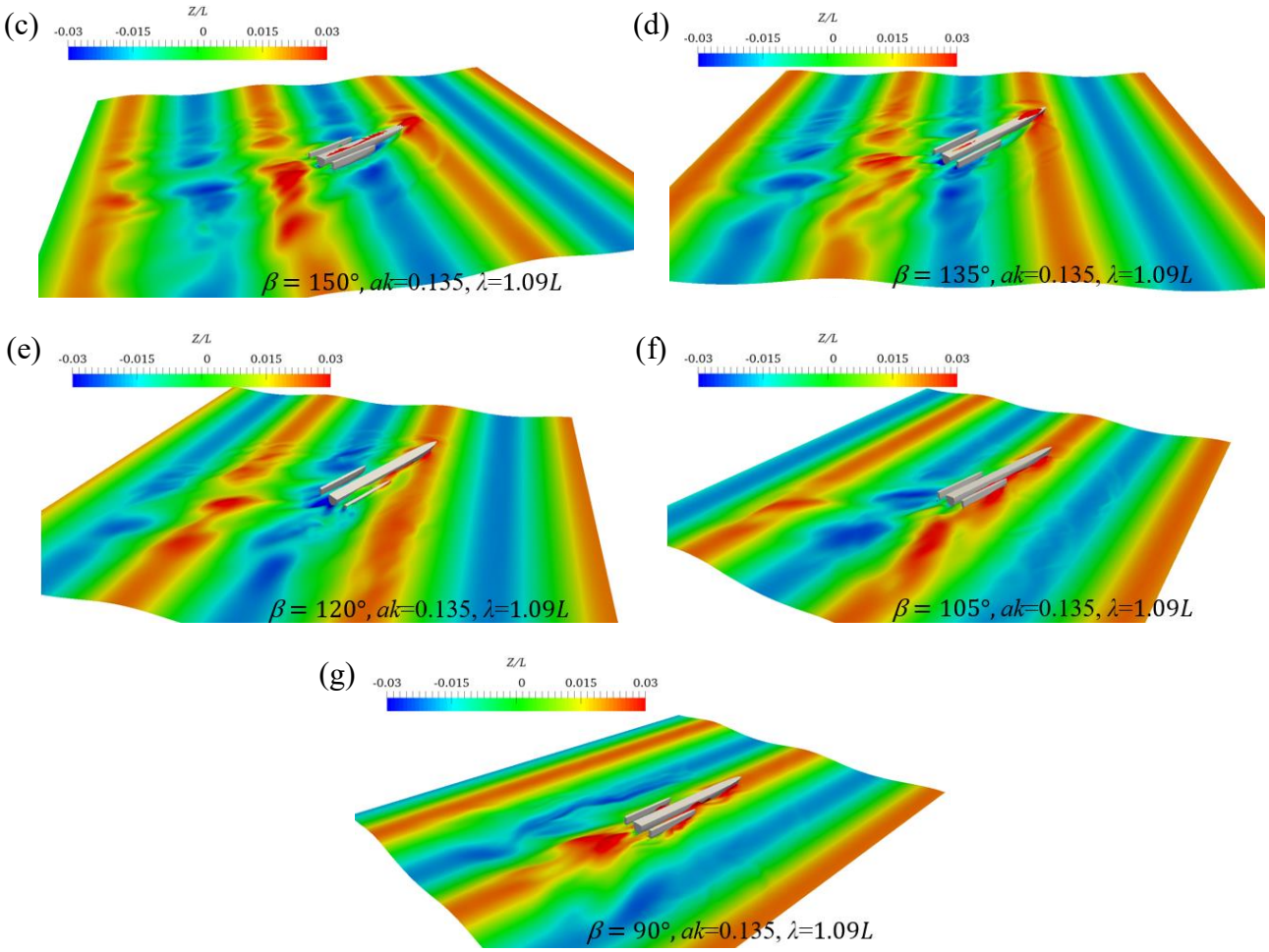

Fig. 18 Snapshots of the free surface around TRI2 with $ak = 0.135$ and $\lambda = 1.09L_{WL}$ when the peak of roll by portside happens. (a) $\beta = 180°$ (b) $\beta = 165°$, (c) $\beta = 150°$, (d) $\beta = 135°$, (e) $\beta = 120°$, (f) $\beta = 105°$, (g) $\beta = 90°$.

Table 7

Parameters for TRI2 moving in different wavelengths

Hull form	Fr	ak	λ/L_{WL}	β (deg)
TRI2	0.35	0.058	0.88 1.09 1.27 1.47	180° – 90°

More snapshots of the free surface around TRI2 at different wave directions with $ak = 0.135$ are shown in Fig. 18, which are captured when the wave peak at the bow of the center hull. From the figure, it can be seen that the amount of green water on the deck is gradually increased with the increase of the incident angle. It can also be seen that the degree of asymmetry of disturbed wave patterns about longitudinal plane of the center hull becomes higher with the decrease of the incident angle up to $\beta = 135°$. Then from $\beta = 120°$, the degree of asymmetry is reduced with the decrease

of the incident angle. This would explain why there is a peak of roll around these angles as observed in Fig. 15(c).

5.2 Effects of different wavelengths

For studying the effects of wavelength, the TRI2 is simulated for the cases of different wavelengths with constant wave steepness ($ak = 0.058$) and different wave directions at $Fr = 0.35$. Based on the fact that the peak value of added resistance appears around $\lambda/L_{WL} = 1.09$, the selected range of the wavelength is from $\lambda/L_{WL} = 0.88$ to $\lambda/L_{WL} = 1.47$. The parameters for the cases considered are given in Table 7.

The computed results are depicted in Fig. 19. It shows that all the quantities near the beam sea are much less sensitive to the wavelength than in the cases with the incident wave angle larger than 100°. When incident wave angle is larger than 120°, the effects of the wavelength are different on different quantities. As seen in Fig. 19(a) , except for $\lambda/L_{WL} = 0.88$, the nondimensionalized added resistance decrease with the increase of wavelength when $\beta \geq 120°$. For $\lambda/L_{WL} = 0.88$, i.e., the wavelength being less than the ship length, the variation of the nondimensionalized added resistance is complicated with a largest value at $\beta = 135°$. Fig. 19(b) shows that the heave motion consistently increases with the wavelength. Fig. 19(c) shows that the roll motion is similar to what has been seen in Fig. 15, that is, there is a peak value in the middle value of incident angle. It also shows that the angle corresponds to the peak tends to be larger for longer waves. The pitch motion for all the wavelengths larger than the ship length is almost the same at all the incident angles but it becomes much smaller for $\lambda/L_{WL} = 0.88$ when the incident angle larger than 135°.

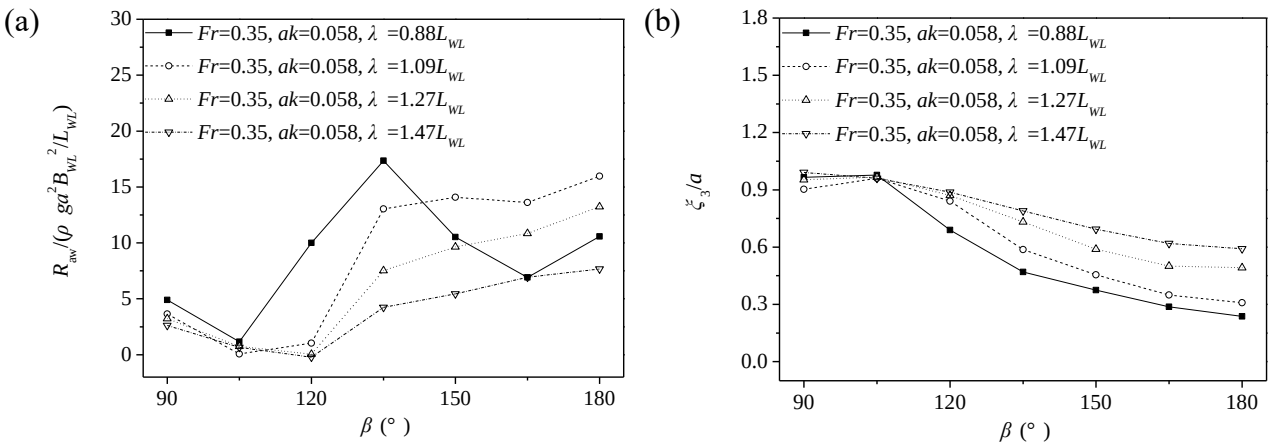

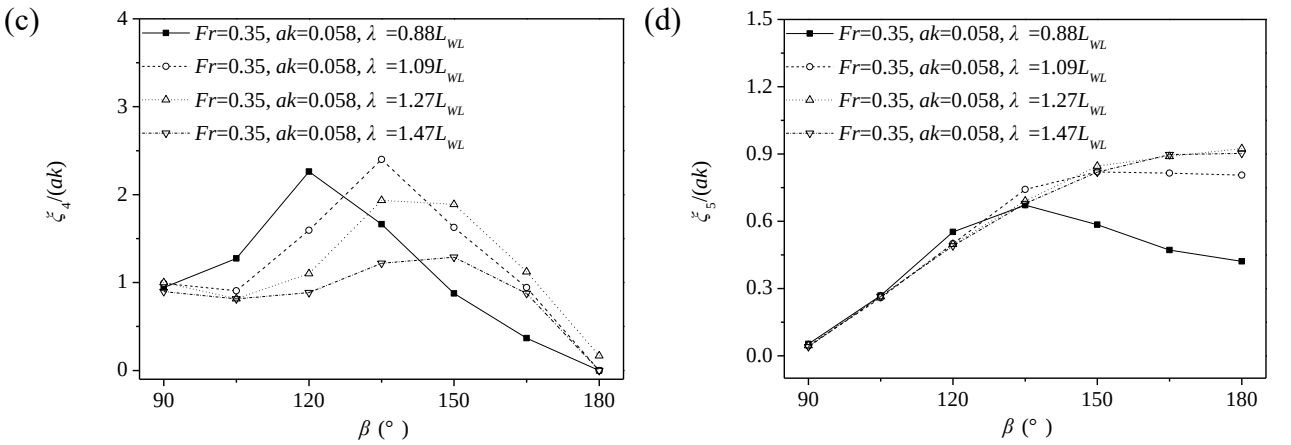

Fig. 19 Computed results for TRI2 for different wavelengths: (a) added resistance, (b) heave amplitudes, (c) roll amplitudes, (d) pitch amplitudes.

Fig. 20 shows the patterns of the nondimensionalized added resistance and motions with the changes of the wavelength and wave direction. It is apparent that, compared with Fig. 16, the patterns here is more complex, especially for the nondimensionalized added resistance and roll motion. There are at least two peak values appears for the added resistance corresponding to the waves longer and shorter than ships, respectively. The area for significant roll lies in $110° \leq \beta \leq 155°$, not at the beam sea. The variation of nondimensionalized heave and pitch is relatively more regular and monotonic.

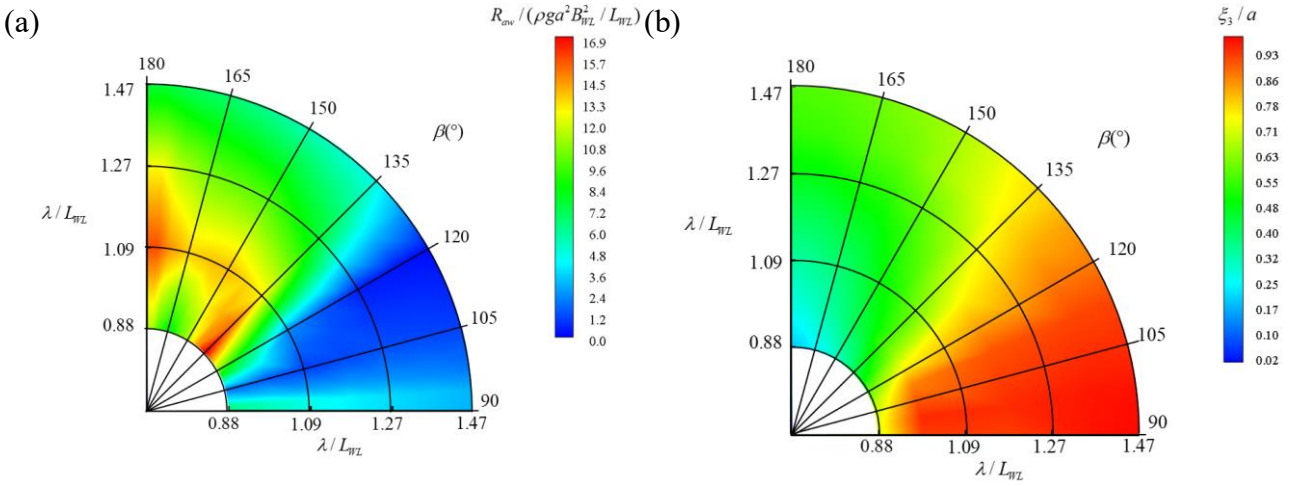

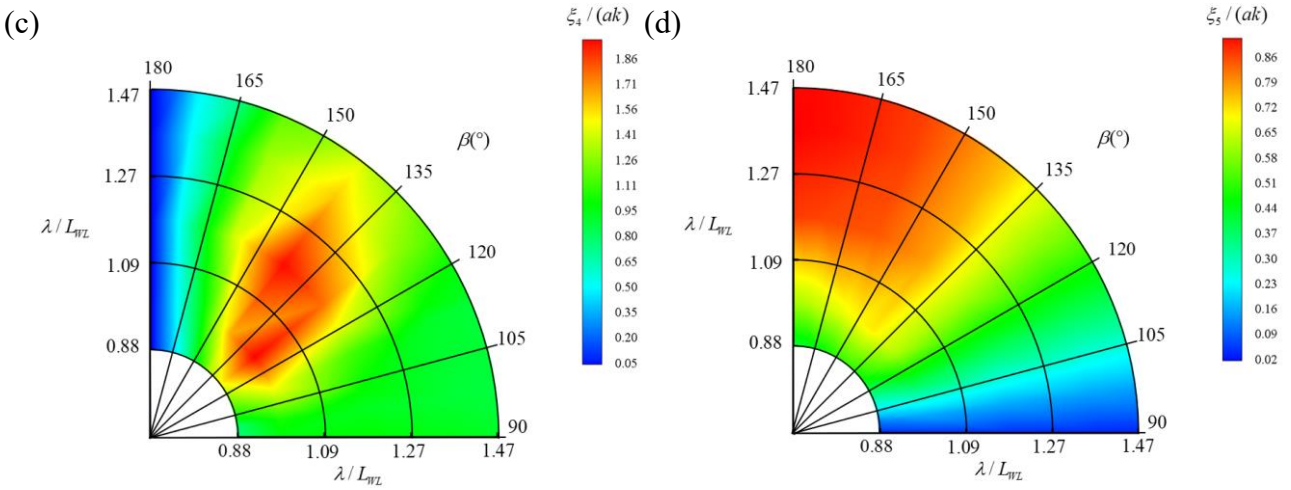

Fig. 20 The added resistance and motion amplitudes of TRI2 in waves with different lengths and directions (constant $ak = 0.058$). (a) added resistance, (b) heave, (c) roll, (d) pitch.

Table 8

Parameters for TRI2 moving at different forward speeds.

Hull form	Fr	ak	λ/L_{WL}	β (deg)
TRI2	0.24, 0.35, 0.47	0.058 0.096 0.135	1.09	180, 135, 90

5.3 Effects of forward speeds

In this section, the effects of forward speeds of the ship will be discussed. For this purpose, the cases with the parameters shown in Table 8 are investigated, where the forward speeds are given as the Froud numbers.

Fig. 21 shows the nondimensionalized added resistance of TRI2 at different Froude numbers. It can be seen that, for the beam sea ($\beta = 90°$), the variational trend of added resistance with the forward speeds is the same at the three values of wave steepness. For the oblique waves ($\beta = 135°$) and head sea, the trend of the added resistance variation with forward speed depends on wave steepness. For the smallest wave steepness ($ak = 0.058$), the largest added resistance occurs at $Fr = 0.35$. In contrast, for the steepest wave ($ak = 0.135$), the largest forward speed ($Fr = 0.47$) leads to the largest added resistance. For the head sea with the steepness of $ak = 0.058$ or 0.135, the largest added resistance is correlated with $Fr = 0.35$, but with $Fr = 0.47$ for $ak = 0.135$.

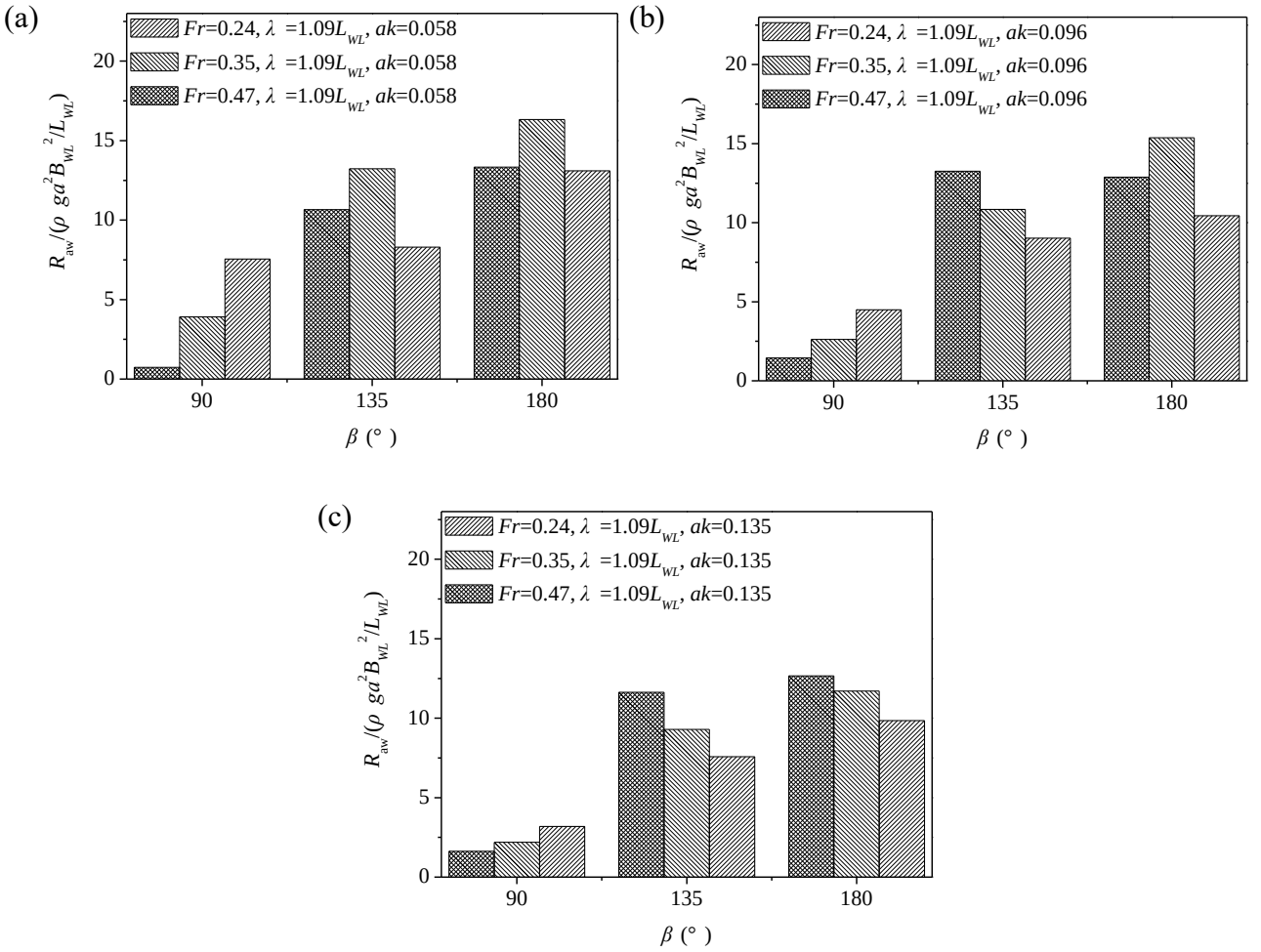

Fig. 21 Computed added resistance of TRI2 with $\lambda/L_{WL} = 1.09$ at different forward speeds. (a) $ak = 0.058$, (b) $ak = 0.096$, (c) $ak = 0.135$.

Fig. 22, Fig. 23 and Fig. 24 depict the nondimensionalized heave, roll and pitch amplitudes of TRI2 with different forward speeds. As shown in the Figures, the forward speed has insignificant influence on the amplitudes of the trimaran at the beam sea ($\beta = 90°$). When $\beta \geq 135°$, the effects of the forward speed is different on heave, roll and pitch amplitudes. The heave amplitude always increases with the forward speed at the wave steepness considered. For the roll amplitudes, when $ak \geq 0.096$, the largest values occurs at the lowest Froude number ($Fr = 0.24$); while for the wave steepness to be 0.058, the largest roll amplitude occurs at the middle Froud number ($Fr = 0.35$). For the pitch amplitudes, the relative importance of the forward speed is similar except for the case with $ak = 0.135$ and $\beta = 135°$. More interesting point is that the largest pitch amplitudes for a value of wave steepness takes place at $\beta = 135°$, rather than $\beta = 180°$, though the corresponding different forward speed could be different.

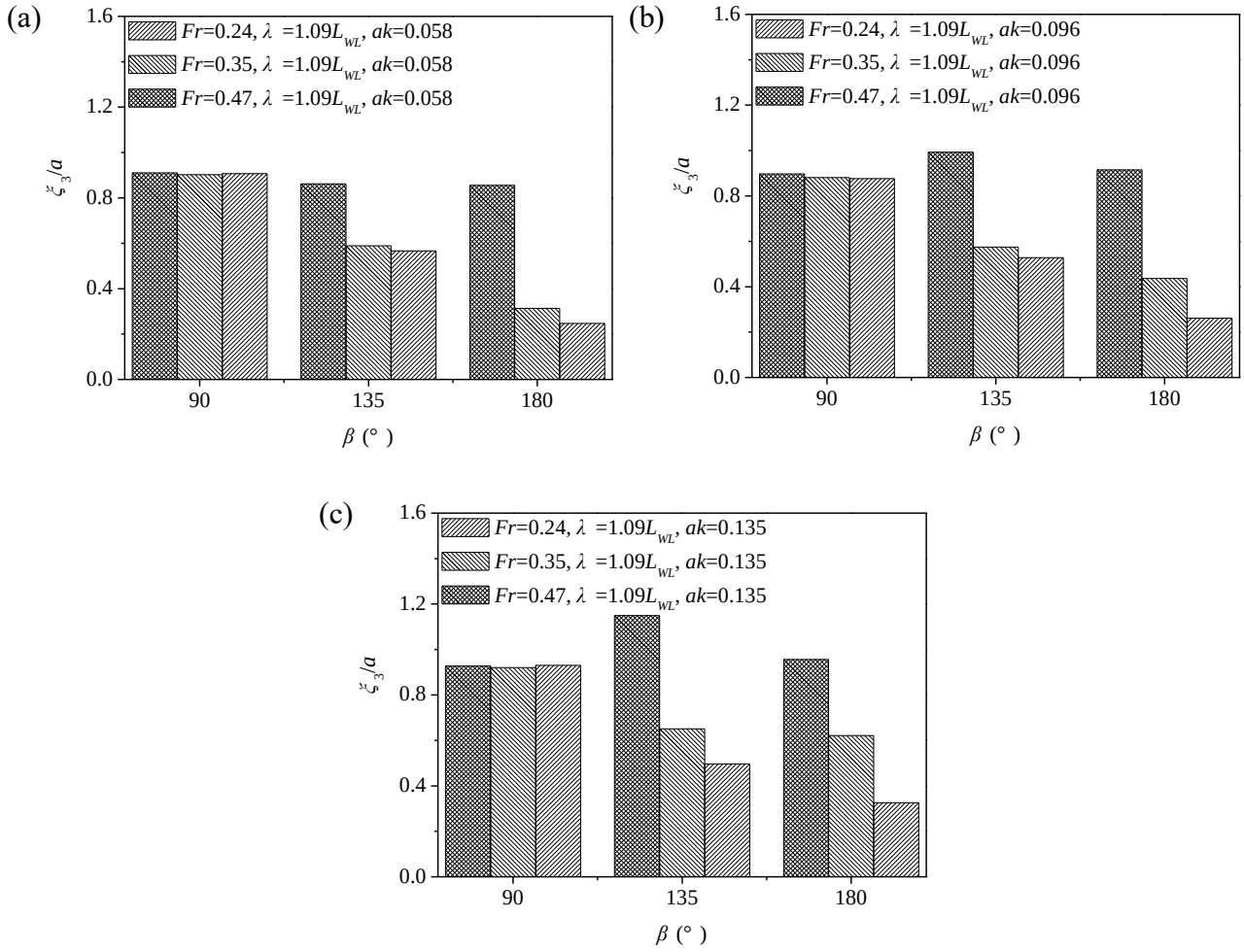

Fig. 22 Computed heave amplitudes of TRI2 with $\lambda/L_{WL} = 1.09$ at different forward speeds. (a) $ak = 0.058$, (b) $ak = 0.096$, (c) $ak = 0.135$.

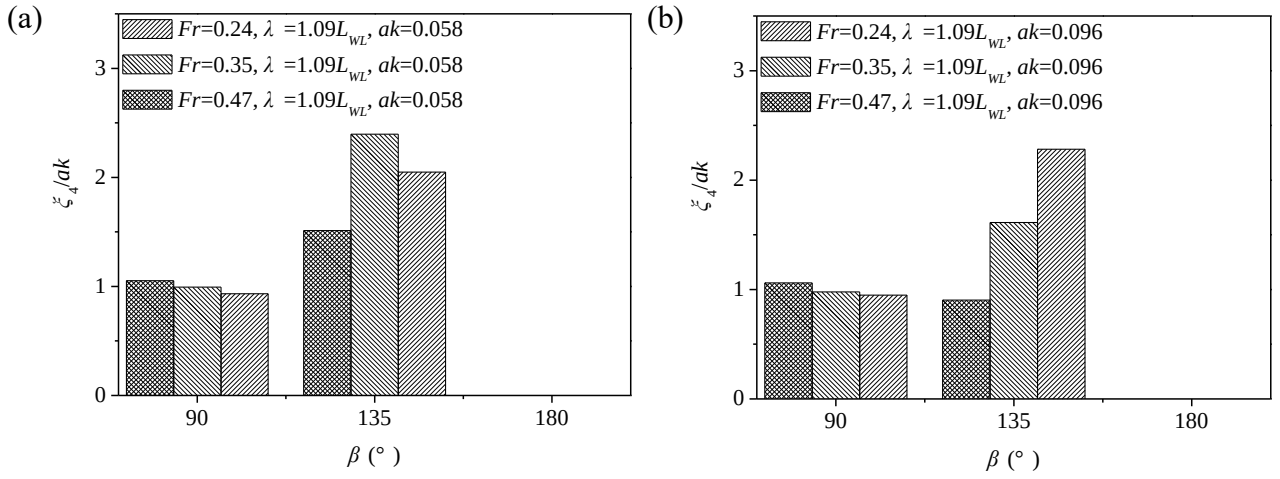

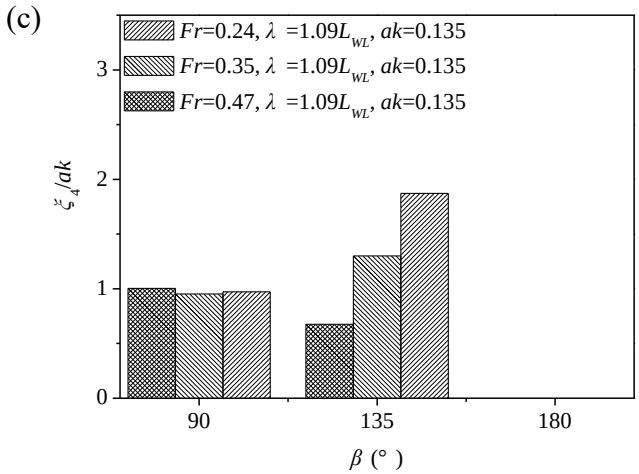

Fig. 23 Computed roll amplitudes of TRI2 with $\lambda/L_{WL} = 1.09$ at different forward speeds (the values at $180°$ being almost zero and so not plotted). (a) $ak = 0.058$, (b) $ak = 0.096$, (c) $ak = 0.135$.

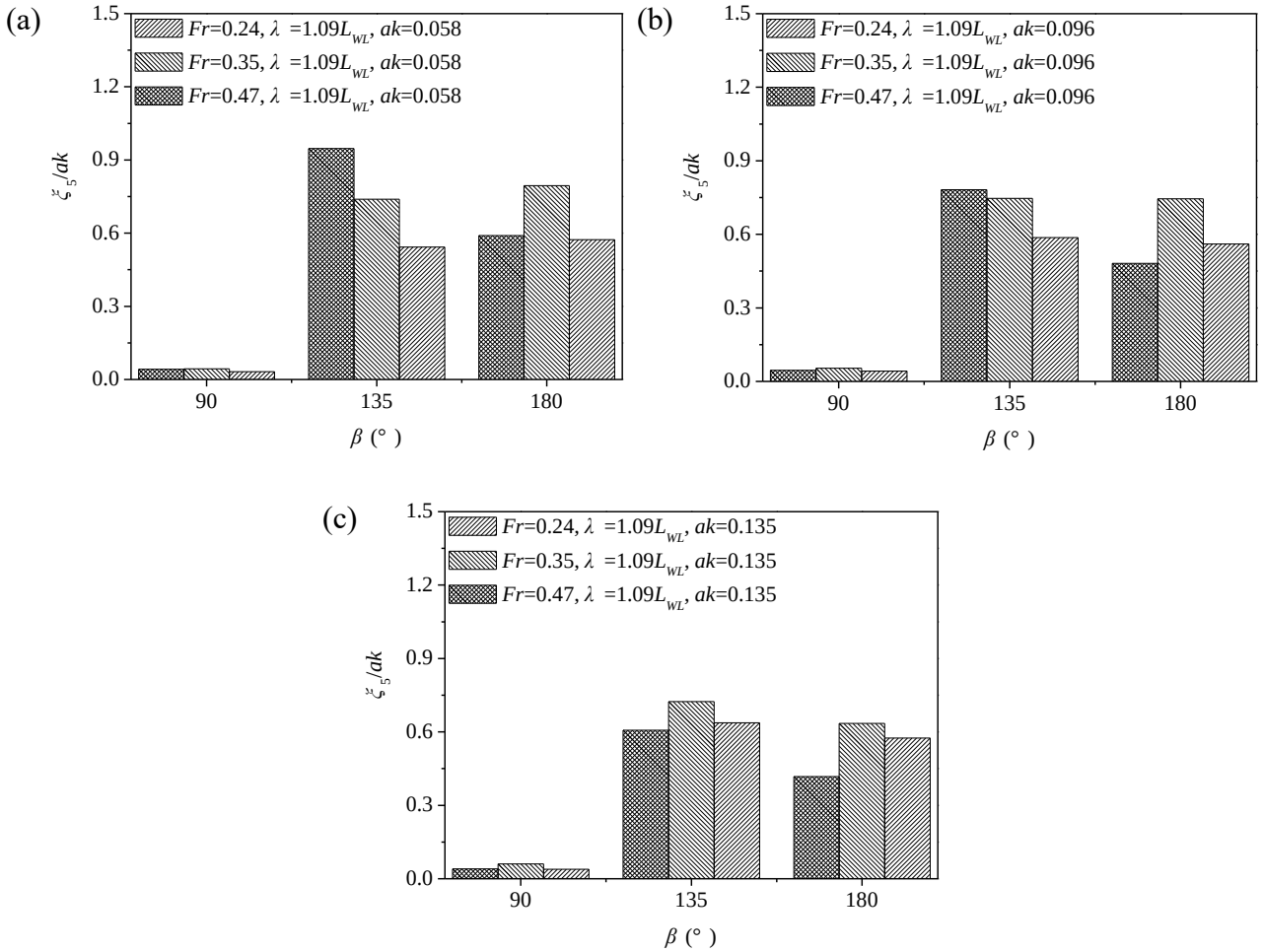

Fig. 24 Computed pitch amplitudes of TRI2 with $\lambda/L_{WL} = 1.09$ at different forward speeds. (a) $ak = 0.058$, (b) $ak = 0.096$, (c) $ak = 0.135$.

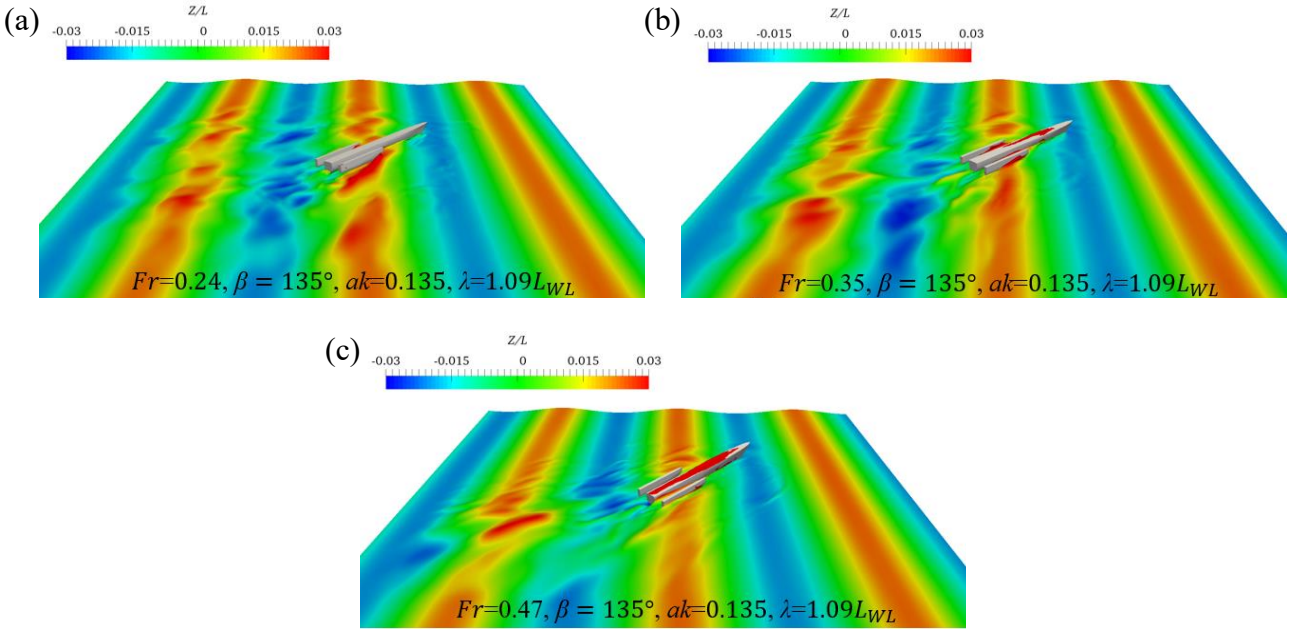

Fig. 25 Snapshots of free surface around TRI2 at different forward speeds with $\lambda/L_{WL} = 1.09$ and $ak = 0.135$. (a) $Fr = 0.24$, (b) $Fr = 0.35$, (c) $Fr = 0.47$.

Fig. 25 shows the snapshots of the free surface around the trimaran at different forward speeds at the moment when the bow at a wave trough. It can be seen that, for the wave steepness of $ak = 0.135$ and the wave angle of $\beta = 135°$, the green water on the deck increase significantly with the forward speed. This is perhaps why the nondimensionalized added resistance and heave increase with the forward speed as have been seen in Fig. 21 (c) and Fig. 22(c).

To reveal more hydrodynamic characteristics of the trimaran, its nondimensionalized added resistance, heave, roll and pitch against forward speed (Froude number) and wavelength for two incident wave angles with the steepness of $ak = 0.058$ are plotted in three dimensional graphs (Fig. 26-Fig. 29), where the two axes represent the Froude number and the ratio of wavelength to ship length, respectively. Fig. 26 shows that the characteristics of the added resistance is very different for the different incident wave angles. For example, the largest added resistance for $\beta = 180°$ occurs at a point where both wavelength and forward speed are quite large ($Fr = 0.47$ and $\lambda/L_{WL} = 1.27$) while it happens, for $\beta = 135°$, at a point of $Fr = 0.24$ and $\lambda/L_{WL} = 0.88$. All such points corresponding to the maxima of added resistance, heave, roll and pitch are collected and plotted in Fig. 30. It is striking to see that all such points locate at the upper left corner above the dashed line through the two points of (0.24, 0.88) and (0.35, 1.27). This may be used as a reference for designing new trimaran or for adjusting forward speed to avoid the maxima occurring.

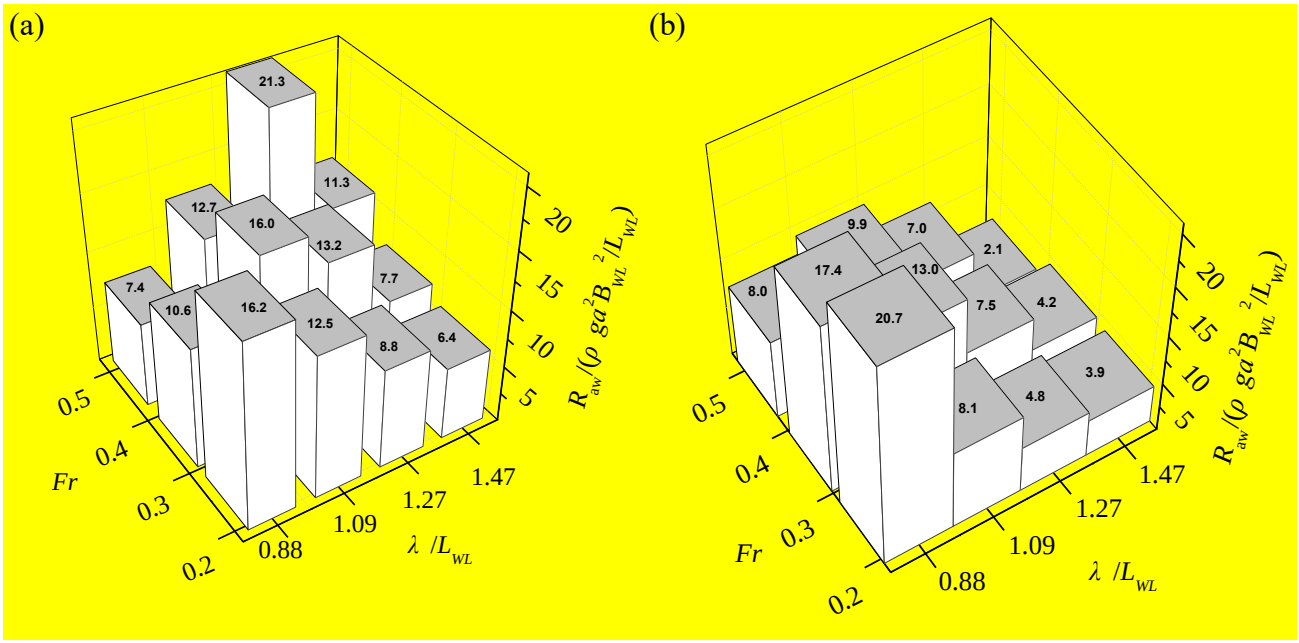

Fig. 26 Computed added resistance of TRI2 with $ak = 0.058$. (a) $\beta = 180°$, (b) $\beta = 135°$. The number on the top of each column indicates the value of nondimensional added resistance it represents.

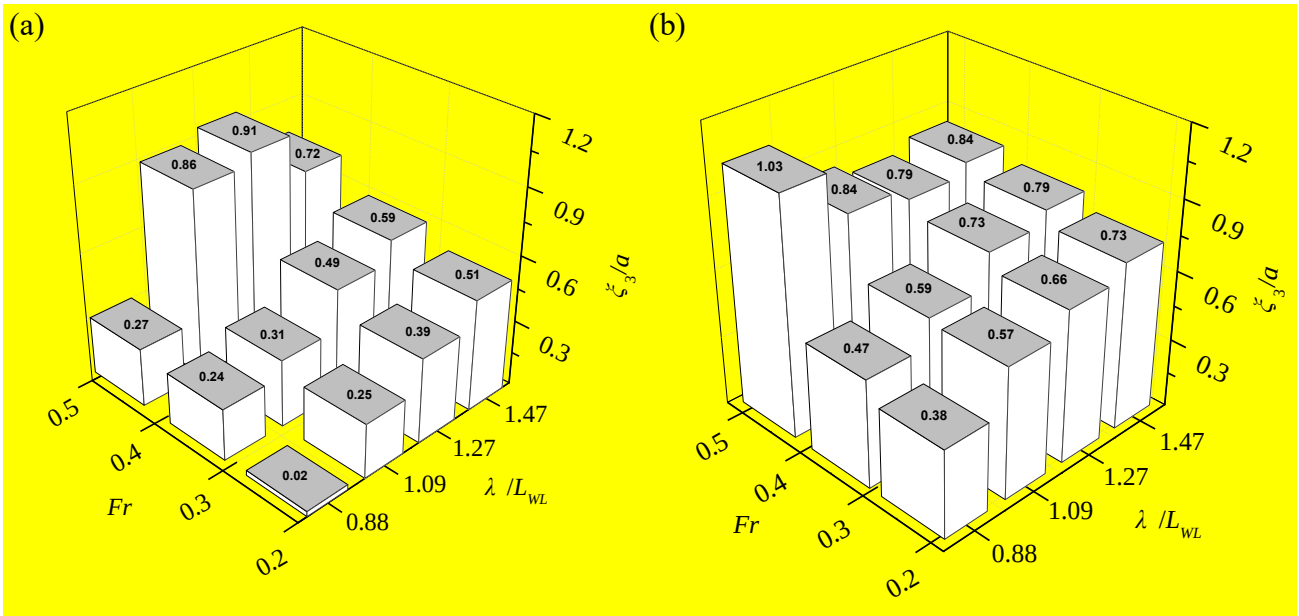

Fig. 27 Computed heave amplitudes of TRI2 with $ak = 0.058$. (a) $\beta = 180°$, (b) $\beta = 135°$. The number on the top of each column indicates the value of nondimensional heave amplitude it represents.

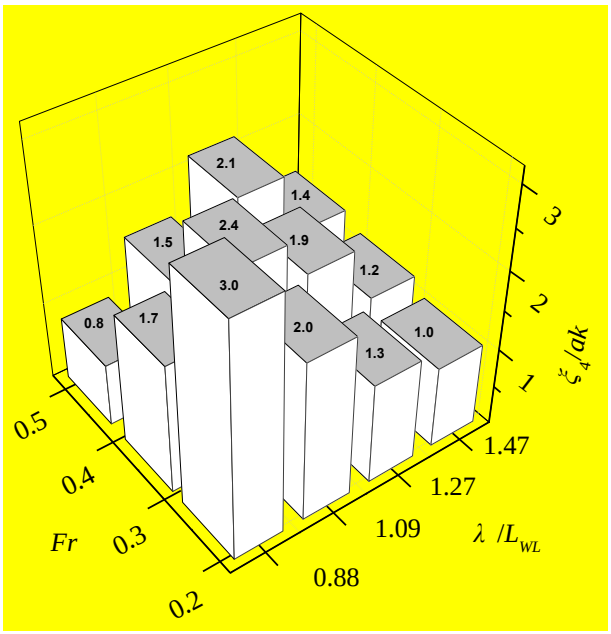

Fig. 28 Computed roll amplitudes of TRI2 with $ak = 0.058$ and $\beta = 135°$. The number on the top of each column indicates the value of nondimensional roll amplitude it represents.

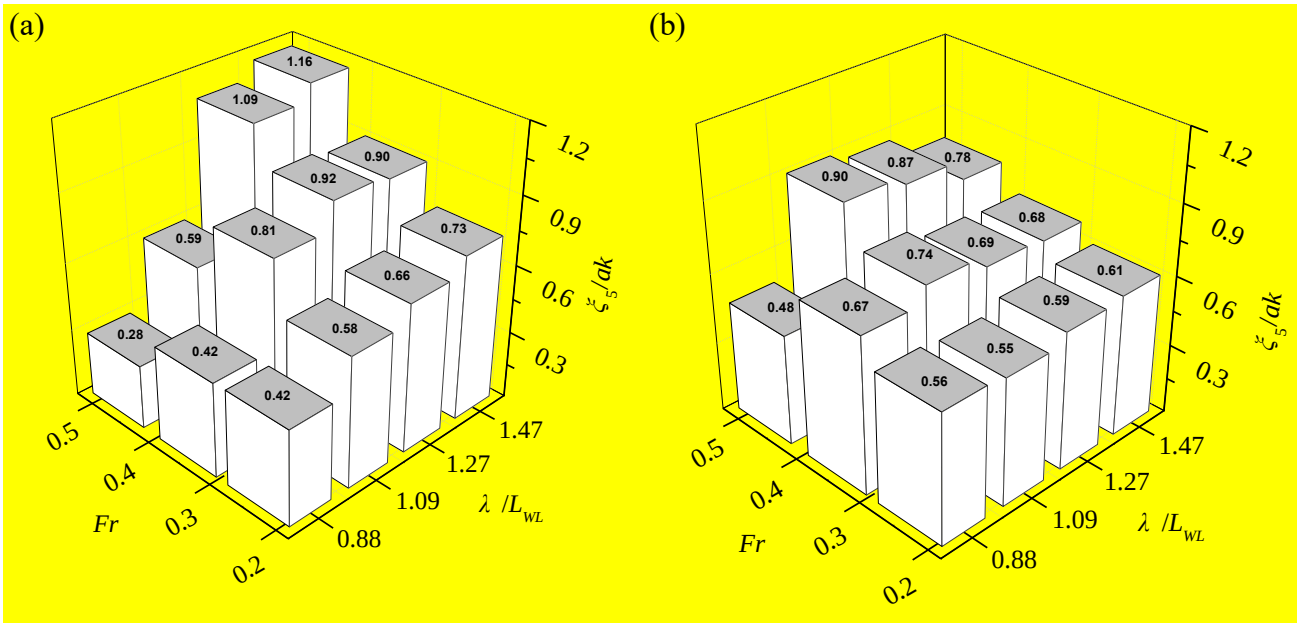

Fig. 29 Computed pitch amplitudes of TRI2 with $ak = 0.058$. (a) $\beta = 180°$, (b) $\beta = 135°$. The number on the top of each column indicates the value of nondimensional pitch amplitude it represents.

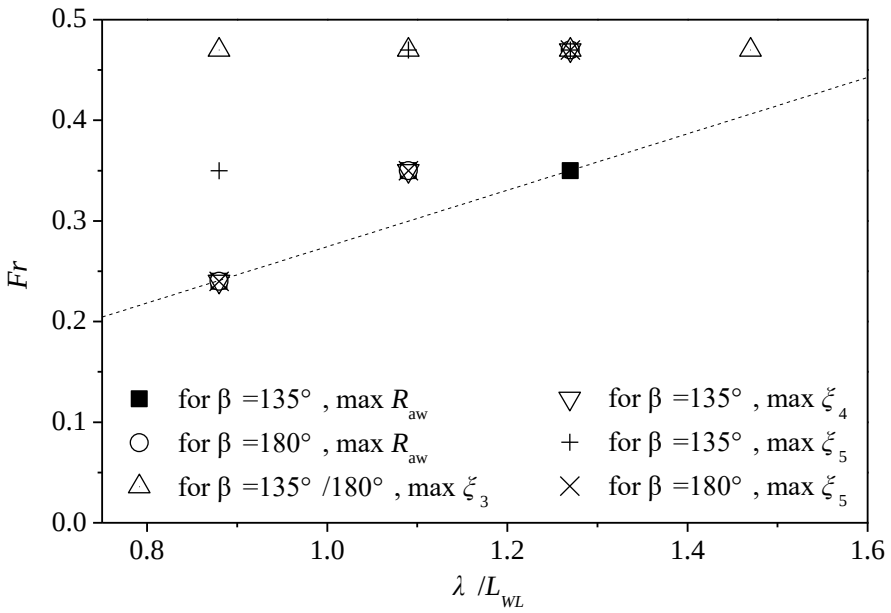

Fig. 30 Froude number and the ratio of wave to ship length corresponding to the maxima of added wave resistance (R_{aw}), heave, roll and pitch amplitudes. (Some points are coincided with and covered by others.)

Another interesting thing to be examined is how the added wave resistance (R_{aw}), heave, roll and pitch amplitudes are correlated with each other. For this purpose, we carry out correlating analysis on all the data in Fig. 26 to Fig. 29, and present the results in Table 9. In this table, the values in the upper right triangle are for $\beta = 180°$ while these on the lower left triangle are for $135°$. It can be seen that the correlation between heave and pitch amplitudes is quite strong, between heave and added wave resistance quite weak, and between pitch and added resistance moderate for the incident wave angle of $180°$. In contrast, for the incident wave angle of $135°$, the correlation between heave and added resistance is quite strong (though negative) but quite weak between pitch and added resistance. For this angle, the roll amplitude is significant as seen in Fig. 28 and is strongly correlated with both heave and added resistance (correlation coefficient around 0.7), but weakly correlated with pitch.

Table 9
Correlation coefficients (the values in the upper triangle for $\beta = 180°$, the lower triangle for $135°$)

	R_{aw}	ξ_3	ξ_4	ξ_5
R_{aw}	1.000	0.185	N/A	0.314
ξ_3	-0.700	1.000	N/A	0.693
ξ_4	0.685	-0.729	1.000	N/A
ξ_5	-0.132	0.181	0.124	1.000

6 Summary and Conclusions

This paper has presented the numerical investigations on the added resistance of a trimaran and motions that mostly affect it in oblique waves under the conditions with different wave steepness, different wavelengths, different forward speeds and different incident wave angles. The investigations are carried out by applying a hybrid method, called as the QaleFOAM, which can simulate a trimaran moving forward in a large 3D wave field and allow strong nonlinear behavior to occur, such as breaking waves, intermittent emergence of side hulls and green water. The method is validated by using experimental results for a trimaran moving in waves, showing a quite good agreement between the numerical and experimental results.

The comparison of two approaches for simulating ship motions in waves is made. One approach often used in literature is that the ship is kept without forward speed while the incident waves and current same as the ship forward speed are assigned at an inlet boundary (named as APP1 in this paper). The second approach used in this paper is to directly simulate the ship moving in the wave field (named as APP2 in the paper). The numerical tests presented here shows that the computed results obtained by the two approaches are almost the same when the wave steepness is small ($ak = 0.058$). However, when the wave steepness is quite large ($ak = 0.135$), the difference between the results obtained by the approaches could be significant. In literature, there is some suspicion on the effect of the interaction between incident waves and the imposed current representing the forward speed in the APP1 but no quantitative information about the effect has been found in literature so far.

The numerical results for the cases considered in systemic investigations indicate the following interesting observations.

(1) The wave steepness significantly affects the added wave resistance and motion amplitudes of the trimaran except for the wave incident angle being near $\beta = 90°$. The difference between the added wave resistance for the smallest and largest steepness studied can be 30%.

(2) In the oblique waves ($\beta = 135°$) and head sea with a fixed ratio of wave to ship length being near 1.09, the trend of the added resistance variation with forward speeds depends on wave steepness. For the smallest wave steepness ($ak = 0.058$) considered, the largest added resistance occurs at $Fr = 0.35$. For the steepest wave ($ak = 0.135$) presented in the paper, the largest added resistance is observed at the largest forward speed ($Fr = 0.47$) studied.

(3) The peak value of roll amplitudes of the trimaran occurs at the wave incident angle near 135°, i.e., in oblique waves, for the given wave steepness or the ratio of wave to ship length,

which is correlated with the asymmetry of the disturbed wave pattern. This is different from the roll behaviors of mono-hull ships, whose largest roll amplitude usually occurs at the beam sea. It is noted that the sway and turbulent effects are not considered in this paper, and that these effects would change the detailed behaviors of roll.

(4) In oblique waves near the incident wave angle of $135°$ the added wave resistance is quite strongly correlated with heave and roll motions, but weakly with pitch motion.

(5) The maxima of added resistance, heave, roll and pitch amplitudes occurs at or above the line going through the two points ($Fr = 0.24,\ \lambda/L_{WL} = 0.88$) and ($Fr = 0.35,\ \lambda/L_{WL} = 1.27$). Using this finding may help avoid the occurrence of the maxima during design and operation. More specific information can be found in Fig. 30.

It is noted that the above observations, not described in the current literature as far as we know, are based only on the cases investigated in the paper. Their applications to a wider range of cases need further investigations.

Acknowledgement

The first author participated in the research work presented in this paper when he was a visiting research student at City, University of London, supported by Chinese Scholarship Council. The second and third authors acknowledge the support of EPSRC grant with reference of EP/M022382/1 and UKIERI grant with reference of DST-UKIERI-2016-17-0029.

Reference

Afshar, M. A., and Bingham, H. B., 2017. Implementation of the far-field method for calculation of added resistance using a high order finite-difference approximation on overlapping grids. The 32nd International Workshop on Water Waves and Floating Bodies, Dalian, China, 23-26 April, 2017.

Brizzolara, S., Capasso, M., Ferrando, M., Bonvino, C. P., and Francescutto, A., 2003. Trimaran Hull Design for Fast Ferry Applications. Int. Conference on Ships Design and Shipping, NAV2003.

Bulian, G., Francescutto, A., and Zotti, I., 2008. Stability and roll motion of fast multihull vessels in beam waves. Ships and Offshore Structures, 3(3), 215-228.

Carrica, P. M., Wilson, R. V., Noack, R. W., and Stern, F., 2007. Ship motions using single-phase level set with dynamic overset grids. Computers & Fluids, 36(9), 1415-1433.

Fang, M. C., 2008. A parametric study of wave loads on trimaran ships traveling in waves. Ocean Engineering, 35(8):749-762.

Guo, B. J., Steen, S., and Deng, G. B., 2012. Seakeeping prediction of KVLCC2 in head waves with rans. Applied Ocean Research, 35(35), 56-67.

Ghadimi, P., Nazemian, A, Ghadimi, A, 2019. Numerical scrutiny of the influence of side hulls arrangement on the motion of a Trimaran vessel in regular waves through CFD analysis. Journal of the Brazilian Society of Mechanical Sciences and Engineering, 41(1).

Hebblewhite, K., Sahoo, P. K., and Doctors, L. J., 2007, A case study: theoretical and experimental analysis of motion characteristics of a trimaran hull form. 5th International Conference on High Performance Marine Vehicles, Australia, 8-10.

Huang, L., Han, Y., Duan, W., Zheng, Y, Ma, S., 2018. Ship pitch-roll stabilization by active fins using a controller based on onboard hydrodynamic prediction. Ocean Engineering, 164, 212-227.

ITTC Recommended Procedures and Guidelines "Uncertainty Analysis in CFD Verification and Validation- Methodology and Validation 7.5-03-01-01" 28th International Towing Tank Conference, 2017.

Issa, R. I., 1986. Solution of the implicitly discretized fluid flow equations by operator-splitting. Comput Phys, 62(1), 40-65.

Jasak, H., 2009. OpenFOAM: Open source CFD in research and industry[J]. International Journal of Naval Architecture & Ocean Engineering, 1(2):89-94.

Khoob, A. A., and Ketabdari M. J., 2017. A numerical investigation into the effects of long-term wave-induced loads on the cross structure of a wave-piercing trimaran. Cogent Engineering.

Kim, M., Hizir, O., Turan, O., Day, S., and Incecik, A., 2017. Estimation of added resistance and ship speed loss in a seaway. Ocean Engineering, 141, 465-476.

Kim, M., Hizir, O., Turan, O., and Incecik, A., 2017. Numerical studies on added resistance and motions of KVLCC2 in head seas for various ship speeds. Ocean Engineering, 140, 466-476.

Kim, M., Jung, K., Park, S., Suh, S., Park, I., Kim, J., Kim, K., 2019. Experimental study on viscous effect in roll and heave motions of a rectangular structure. Ocean Engineering, 171, 250-258.

Kurultay, A. A., 2003. Sensitivity analysis of the seakeeping behavior of trimaran ships. Monterey, California. Naval Postgraduate School.

Li, Q., Wang, J. H., Yan, S. Q., Gong, J. Y., and Ma, Q. W., 2018. A zonal hybrid approach coupling FNPT with OpenFOAM for modelling wave-structure interactions with action of current.

Ma, Q. W., and Yan, S. Q., 2009. QALE-FEM for numerical modelling of non-linear interaction between 3D moored floating bodies and steep waves. International Journal for Numerical

Methods in Engineering, 78(6), 713-756.

Ma, Q. W., Yan, S., Greaves, D., Mai, T., Raby, A., 2015. Numerical and experimental studies of Interaction between FPSO and focusing waves. The Twenty-fifth International Ocean and Polar Engineering Conference, Kona, Hawaii, USA.

Ma, S., Duan, W. Y., and Song, J. Z., 2005. An efficient numerical method for solving '2.5D' ship seakeeping problem. Ocean Engineering, 32(8), 937-960.

Ma, S., Duan, W. Y., Wang, B., and Wang, R. F., 2012. Prediction of ship motions of trimaran in oblique regular wave. Chinese Journal of Hydrodynamics, 27(2), 224-230.

Mizoguchi, S., and Tasaki, R., 1981. Motions of a high-speed container ship in regular oblique waves. Journal of the Kansai Society of Naval Architects Japan, 13-23.

Min, X. U., and Zhang, S. L., 2011. A numerical study on side hull optimization for trimaran. Journal of Hydrodynamics, Ser. B, 23(2), 265-272.

Nowruzi, L, Enshaei, H, Lavroff J, Kianejad SS, Davis MR. 2020a. CFD simulation of motion responses of a trimaran in regular head waves. Int J Marit Eng. 162:91–106.

Nowruzi, L, Enshaei, H, Lavroff J, Kianejad SS, Davis MR. 2020b. Parametric study of seakeeping of a trimaran in regular oblique waves, Ships and Offshore Structures, DOI: 10.1080/17445302.2020.1735809.

Onas, A., and Datla, R., 2011. Non-linear roll motions of a frigate-type trimaran. Proceedings of the 11th International Conference on Fast Sea Transportation, 26-29.

Orihara, H., and Miyata, H., 2003. Evaluation of added resistance in regular incident waves by computational fluid dynamics motion simulation using an overlapping grid system. Journal of Marine Science & Technology, 8(2), 47-60.

Park, D.M., Lee, J.H., Jung, Y.W., Lee, J., Kim, Y., Gerhardt, F., 2019. Experimental and numerical studies on added resistance of ship in oblique sea conditions. Ocean Eng., 186 (2019), p. 106070.

Pastoor, W., Veer, R., and Harmsen, E., 2004. Seakeeping behavior of a frigate-type Trimaran. Design & Operation of Trimaran Ships, London, UK.

Pattison, D.R., and Zhang, J.W., 1994. The Trimaran Ships'. Paper No. 1, RINA Spring Meeting, April, 1994.

Ransley, E., Yan, S., Brown, S., Mai, T., Graham, D., Greaves, D.,Ma, Q., Musiedlak, P.-H., Engsig-Karup, A. P., Eskilsson, C., Li, Q.,Wang, J., Xie, Z., Sriram, V., Stoesser, T., Zhuang, Y., Li, Q., Wan, D., Chen, G., Chen, H., Qian, L., Ma, Z., Causon, D., Mingham, C., Gatin, I., Jasak, H., Vukˇcevi´c, V., Downie, S., Higuera, P., Buldakov, E., Stagonas, D., Chen, Q., Zang, J. (2019). "A blind comparative study of focused wave interactions with a fixed FPSO-like structure (CCP-WSI Blind Test Series 1)", International Journal of Offshore and Polar

Engineering, Vol. 29, pp. 113-128.

Rhie, C. M., and Chow, W. L., 1983. Numerical study of the turbulent flow past an airfoil with trailing Edge separation, AIAA J, 21(11), 1525-1532.

Roache, P. J., 1994. Perspective: a method for uniform reporting of grid refinement studies. Journal of Fluids Engineering, 116(3), 405-413.

Roache, P. J., 1998. Verification and validation in computational science and engineering, 6(5), 8-9.

Rusche, H., 2002. Computational Fluid Dynamics of Dispersed Two-Phase Flows at High Phase Fractions.

Riesner, M., and Moctar, O., 2018. A time domain boundary element method for wave added resistance of ships taking into account viscous effects. Ocean Engineering, 162(2018), 290-303.

Sadathosseini, H., Wu, P. C., Carrica, P. M., Kim, H., Toda, Y., and Stern, F., 2013. CFD verification and validation of added resistance and motions of KVLCC2 with fixed and free surge in short and long head waves. Ocean Engineering, 59(1), 240-273.

Sato, Y., Orihara, H., and Miyata, H., 2006. Practical application of two CFD codes for ship motions in arbitrary waves. 26th Symposium on Naval Hydrodynamics Rome, Italy, 17-22.

Sato, Y., Uzawa, K., and Miyata H., 2007. Validation of motion prediction method for Trimaran vessels. 9th International Conference on Numerical Ship Hydrodynamics Michigan, U.S.A., 5-8.

Shen, Z. R., and Wan, D. C., 2013. RANS computations of added resistance and motions of a ship in head waves. International Journal of Offshore and Polar Engineering, 23(4), 263-271.

Shen, Z. R., Ye, H. X., and Wan, D. C., 2014. URANS simulations of ship motion responses in long-crest irregular waves. Journal of Hydrodynamics, 26(3), 436-446.

Sigmund, S., and Moctar, O., 2018. Numerical and experimental investigation of added resistance of different ship types in short and long waves. Ocean Engineering, 147(2018), 51-67.

Simonsen, C. D., Otzen, J. F., Joncquez, S., and Stern, F., 2013. EFD and CFD for KCS heaving and pitching in regular head waves. Journal of Marine Science and Technology, 18(4), 435-459.

Skejic, R., and Faltinsen, O. M., 2008. A unified seakeeping and maneuvering analysis of ships in regular waves. Journal of Marine Science & Technology, 13(4), 371-394.

Sprenger, F., Maron, A., Delefortrie, G., Van Zwijnsvoorde, T., Cura-Hochbaum, A., Lengwinat, A., Papanikolaou, A., 2017. Experimental studies on seakeeping and maneuverability in adverse conditions. J. Ship Res. 61, 131–152.

Wang, J., Ma, Q. and Yan, S., 2018. A fully nonlinear numerical method for modeling wave–current interactions. Journal of Computational Physics, 369. 173–190.

Wang, S., Khoo, B. C., Liu, G. R., and Xu, G. X., 2013. An arbitrary Lagrangian–Eulerian gradient smoothing method (GSM/ALE) for interaction of fluid and a moving rigid body. Computers and

Fluids, 71(3), 327-347.

Weller, H. G., 2002. Derivation, modelling and solution of the conditionally averaged two-phase flow equations.

Walree, F. V., and Jong, P. D., 2008. Time domain simulations of the behaviour of fast ships in oblique seas. Proceedings of the 10th International Ship Stability Workshop, 23-25 March 2008, Daejeon, Republic of Korea.

Weymouth, G. D., Wilson, R. V., and Stern, F., 2005. Rans computational fluid dynamics predictions of pitch and heave ship motions in head seas. Journal of Ship Research, 49(49), 80-97.

Wu, C. S., Zhou, D. C., Gao, L., and Miao, Q. M., 2011. CFD computation of ship motions and added resistance for a high speed trimaran in regular head waves. Shipbuilding of China, 3(1), 105-110.

Xing, T., Carrica, P., and Stern, F. ,2008. Computational towing tank procedures for single run curves of resistance and propulsion. Journal of Fluids Engineering, 130(10), 1135-1150.

Xia, K., Zhan, M., Wan, D., and Wei, G. W., 2012. Adaptively deformed mesh based interface method for elliptic equations with discontinuous coefficients. Journal of Computational Physics, 231(4), 1440-1461.

Yan, S. Q., and Ma, Q. W., 2007. Numerical simulation of fully nonlinear interaction between steep waves and 2D floating bodies using the QALE-FEM method. Journal of Computational Physics, 221(2), 666-692.

Yan, S. Q., and Ma, Q. W., 2010. QALE-FEM for modelling 3D overturning waves. International Journal for Numerical Methods in Fluids, 63(6), 743-768.

Yan, S., Ma, Q.W., 2017. A hybrid approach coupling MLPG-R with QALE-FEM for modelling fully nonlinear water waves. Proceedings of the 27th International Offshore and Polar Engineering Conference, San Francisco, USA.

Yan, S., Wang, J.H., Wang, J.X., Ma, Q.W., Xie, Z.H, 2019. Numerical Simulation of Wave Structure Interaction using QaleFOAM, Proceedings of the 29th International Offshore and Polar Engineering Conference, Honolulu, Hawaii, USA.

Zhang, J.W., 1997. Design and hydrodynamic performance of trimaran displacement ships. PhD Thesis, University College London, London, UK.